Cell Reports
Medicine

Article

AI-driven multimodal algorithm predicts immunotherapy and targeted therapy outcomes in clear cell renal cell carcinoma

Graphical abstract

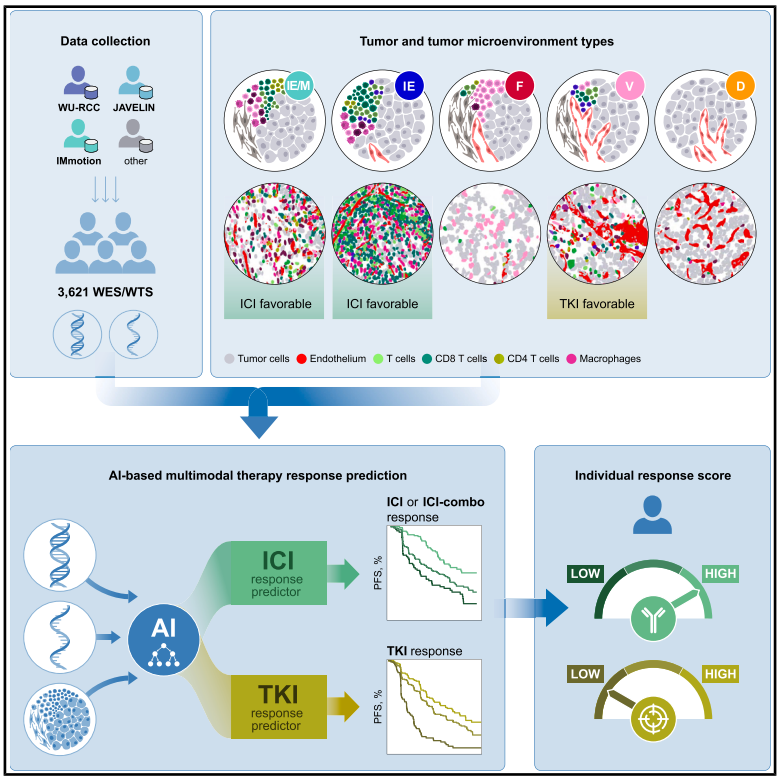

Highlights

- Multimodal AI-based ICI and TKI response prediction models
- Curation of the largest known harmonized ccRCC transcriptomic database
- Prognostic and predictive ccRCC tumor microenvironment subtypes for therapy response
- An integrated decision-tree model to guide ICI and TKI therapy selection

Authors

Danil Stupichev, Natalia Miheecheva, Ekaterina Postovalova, ..., Emily Cheng, Alexander Bagaev, James J. Hsieh

Correspondence

aleksander.bagaev@bostongene.com (A.B.),
jhsieh@wustl.edu (J.J.H.)

In brief

Stupichev et al. present the largest known harmonized clear cell renal cell carcinoma (ccRCC) transcriptomic database, uncovering five distinct transcriptomic subtypes. With these findings, they design multimodal AI models for predicting immunotherapy and tyrosine kinase inhibitor response in patients with ccRCC, ultimately developing an integrated decision-tree model for treatment selection.

Stupichev et al., 2025, Cell Reports Medicine 6, 102299
August 19, 2025
https://doi.org/10.1016/j.xcrm.2025.102299

CellPress

Cell Reports Medicine

CellPress
OPEN ACCESS

Article

AI-driven multimodal algorithm predicts immunotherapy and targeted therapy outcomes in clear cell renal cell carcinoma

Danil Stupichev,[1] Natalia Miheecheva,[1] Ekaterina Postovalova,[1] Yang Lyu,[2] Akshaya Ramachandran,[2] Ilya Galkin,[1] Gleb Khegai,[1] Kristina Perevoshchikova,[1] Anna Love,[1] Sofia Menshikova,[1] Artem Tarasov,[1] Viktor Svekolkin,[1] Maria Bruttan,[1] Arina Varlamova,[1] Kirill Kriukov,[1] Ravshan Ataullakhanov,[1] Nathan Fowler,[1] Emily Cheng,[3] Alexander Bagaev,[1,4,*] and James J. Hsieh[2,*]

[1]BostonGene Corporation, Waltham, MA 02453, USA
[2]Department of Medicine, Washington University, St. Louis, MO 63110, USA
[3]Human Oncology and Pathogenesis Program and Department of Pathology, Memorial Sloan Kettering Cancer Center, New York, NY 10065, USA
[4]Lead contact
*Correspondence: aleksander.bagaev@bostongene.com (A.B.), jhsieh@wustl.edu (J.J.H.)
https://doi.org/10.1016/j.xcrm.2025.102299

SUMMARY

Treatment for metastatic clear cell renal cell carcinoma (ccRCC) has dramatically advanced with tyrosine kinase inhibitor (TKI) and immune checkpoint inhibitor (ICI) administration. However, most patients eventually succumb to their disease, and toxicities associated with individual treatment modalities are significant. Multiple single-modality transcriptomic signatures have been developed to predict treatment response, yielding insightful yet inconsistent results when applied to independent cohorts. By unifying transcriptomic data from 14 cohorts (total n = 3,621), we present harmonized immune tumor microenvironment (HiTME) ccRCC subtypes validated with spatial proteomics. This AI-based multimodal approach integrates genomic, transcriptomic, and tumor microenvironment (TME) features for ICI and TKI therapy response prediction.

INTRODUCTION

Antiangiogenics (AAs), including vascular endothelial growth factor receptor 2 (VEGFR2) tyrosine kinase inhibitors (TKIs) and anti-vascular endothelial growth factor (VEGF) antibodies, and cytotoxic T-lymphocyte associated protein 4 (CTLA4) and programmed cell death protein 1 (PD1) immune checkpoint inhibitors (ICIs), have broadened the treatment landscape for patients with metastatic clear cell renal cell carcinoma (ccRCC),[1,2] with overall response rates between 55% and 70% in ICI+TKI clinical trials.[3–5] While the emergence of ICI+TKI treatment improved outcomes, no reliable biomarkers currently exist to guide treatment decisions and to distinguish ICI responders (Rs) from non-responders (NRs). Previous reports confirmed that tumor mutational burden (TMB), programmed death-ligand 1 (PDL1) expression, $CD8^+$ T cell content, mutational profiles, histology, and gene signatures are insufficient for identifying potential TKI and ICI therapy Rs.[6–11] Several transcriptomic signatures and classifications, including JAVELIN Renal 101 (JAVELIN), IMmotion150, IMmotion151, and CheckMate214,[6,9–14] have been associated with treatment outcomes. However, the prognostic values of these signatures are inconsistent on external datasets except IMmotion150 Angio,[9,13] which is a positive prognostic factor for both ICI+AA and AA treatment arms.[8] These limitations indicate a need for improved multimodal biomarker schemes that can predict TKI and ICI response, underscoring the importance of a meta-cohort analysis.

We applied a machine learning (ML)-based integrative genomic, transcriptomic, and tumor microenvironment (TME) approach to yield more accurate multimodal white-box predictive signatures for discerning ICI and TKI Rs and NRs. A harmonized transcriptomic database of 3,621 ccRCC samples was compiled to characterize the TME landscape. Harmonized immune TME (HiTME) subtypes were defined with functional gene expression signature (FGES) density-based clustering.[15] These HiTME subtypes were subsequently validated with multiplex immunofluorescence (MxIF) and used as the foundation for AI training.

Multimodal AI models were developed to estimate TKI and ICI therapy response across a harmonized meta-cohort. An independent validation cohort from Washington University (WU-RCC, n = 193)[16] was assembled to evaluate model generalizability. The developed ccRCC TKI and ICI response scores were subsequently translated into a clinical therapy selection scheme to maximize patient outcomes.

RESULTS

Characteristics of the WU-RCC cohort

The genomic and transcriptomic factors influencing TKI and ICI response were assessed on a ccRCC cohort (WU-RCC,

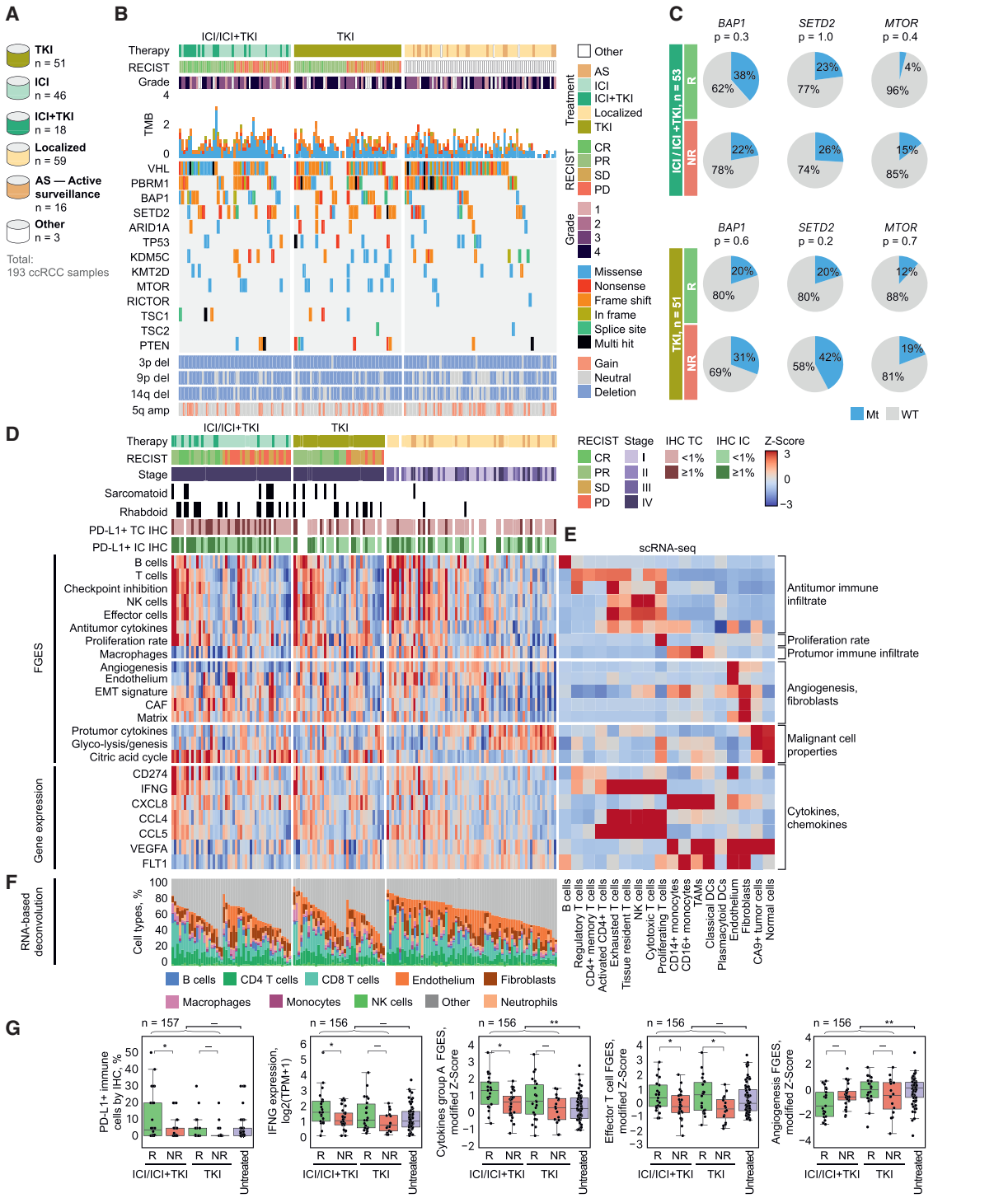

Figure 1. Characteristics of the WU-RCC cohort

(A) Therapy distribution among WU-RCC ccRCC samples (n = 193).[16]

(B) Oncoplot of alterations among WU-RCC ccRCC samples (n = 176) with tumor mutational burden (TMB, mut/Mb), copy number alteration of chromosome arms, therapy, RECIST, and grade.

(C) Pie charts for *BAP1*, *SETD2*, and *MTOR* alterations among responders (Rs; CR + PR) and nonresponders (NRs; SD + PD) treated with ICI/ICI+TKI (n = 53 total; 26 Rs and 27 NRs) and TKI (n = 51 total; 25 Rs and 26 NRs) therapies and untreated WU-RCC ccRCC patients. Chi-square test.

(D) FGES and cytokine expression in WU-RCC ccRCC samples with bulk RNA-seq data (n = 157). Tumor stage, histology, and PDL1 IHC for tumor cells (TCs) and immune cells (ICs) were annotated.

(legend continued on next page)

n = 193)[16] from Washington University School of Medicine in St. Louis. Patients with metastatic renal cell carcinoma (RCC) were subdivided by first-line therapies: TKIs, ICIs, or ICI+TKI combinations (Figure 1A; Table S1; STAR Methods). DNA sequencing was performed to characterize mutational profiles (Figures 1B, S1A, and S1B). Interestingly, *MTOR*-mutated patients were less responsive to ICIs, while *BAP1*- and *SETD2*-mutated patients were less responsive to TKIs (Figure 1C). As previously reported,[17] 9p and 14q loss were associated with metastasis (Figure S1C). Genomic findings, including TMB, were not significant among Rs and NRs (Figures 1C, S1A, and S1B), defined as NR with stable (SD) and progressive (PD) disease, and as Rs with complete (CR) and partial (PR) responses.

FGES analysis[15] uncovered distinct patient groups with high expression of antitumor and protumor immune infiltrate, angiogenic and fibroblastic features, or malignant cell and metabolic properties (Figure 1D). FGESs measured from bulk RNA sequencing (RNA-seq) were validated with single-cell RNA-seq (scRNA-seq; Figures 1E and S1D). T and natural killer (NK) cells were associated with FGES of antitumor immune infiltrate, while monocytes, tumor-associated macrophages (TAMs), and dendritic cells expressed protumor immune infiltrate FGESs (Figure 1E). scRNA-seq revealed that activated T cells expressed cytokines (*CCL4* and *CCL5*) associated with ICI response.[22] Myeloid populations expressed suppressive *CXCL8* (interleukin-8),[23] while epithelial cells expressed elevated metabolic signatures.

RNA-based deconvolution was performed using Kassandra[21] to determine the TME cellular composition (Figure 1F). Decreased endothelial cell proportions in ICI Rs were the only significant finding (Figure S1E). Still, ICI and TKI Rs had increased effector T cell FGESs (Figures 1G and S1F).[15] PDL1 expression on immune cells, but not cancer cells, was also significantly higher in ICI Rs. Interestingly, angiogenesis FGESs[15] could not distinguish Rs from NRs in either treatment arm (Figures 1G and S1G). Similarly, cancer-associated fibroblast (CAF), epithelial-mesenchymal transition (EMT), and myeloid FGESs[15] were not significantly different among any treatment groups, but ICI Rs expressed stronger proliferation FGES (Figures 1G and S1G). *IFNG* and a cytokine signature (*CCL4*, *CCL5*, *CXCL1*, *CXCL13*, *CD274*, and *TNFSF13B*)[22] were increased among ICI Rs (Figure 1G). Additional analyses of *VEGFA*, *PDCD1*, *FLT1*, and *CXCL8* were not statistically significant, but *UTS2* was significantly higher in ICI Rs (Figure S1H). These results showed that individual biomarkers and signatures could not distinguish Rs from NRs. To address this limitation, we conducted a meta-analysis harmonizing independent published ccRCC cohorts.

Developing an expansive ccRCC transcriptome database for HiTME subtype characterization

We compiled the largest transcriptomic collection of ccRCC samples to date (4,187 samples from 17 databases, including cancer research consortiums, ccRCC studies, and clinical trials; Figures 2A and S2; Tables S2 and S3). Data from all stages, primary and metastatic samples, and RNA-seq and microarray platforms were included. In total, we collected 11 immiscible batches, which were scaled after single-sample gene set enrichment analysis (Figure 2B).[15] For 3,621 samples, we measured 33 normalized FGES scores[15,24] encompassing multiple aspects of ccRCC biology (STAR Methods, Figure 2C; Table S4). FGES density-based unsupervised clustering was applied to define five HiTME subtypes: IE/M (immune-enriched, myeloid immunosuppressive), IE (immune-enriched, nonfibrotic), F (fibrotic-myeloid immunosuppressive), V (highly vascularized), and D (immune desert, Figures 2B and 2C).[15] IE samples presented strong immune infiltrate and moderately high metabolic FGESs. While low in metabolic FGESs, IE/M samples expressed elevated levels of CAF, extracellular matrix (ECM), and myeloid-suppressive FGESs, similar to F HiTMEs. F HiTMEs expressed strong myeloid immune infiltrate FGESs associated with protumor cytokines, myeloid-derived suppressor cells, macrophages, CAFs, and EMT. Fibrotic HiTMEs (IE/M and F) also shared high proliferation FGES. Cold HiTMEs included subtype V, enriched with angiogenic, endothelium, CAF, ECM-related, and EMT FGESs, and subtype D with strong glycolysis, citric acid cycle, and fatty acid metabolism FGESs, indicative of enhanced metabolism (Figure 2C).

Cell content examination revealed high levels of $CD8^+$ T cells in IE and IE/M HiTMEs, though IE/M HiTME additionally contained $CD4^+$ T and B cells (Figure 2D). IE and IE/M had similar profiles for checkpoint molecules and cytokines, except *CD274* and *CXCL8*, which were higher in subtypes IE and IE/M, respectively. F HiTME also showed high *CXCL8* levels, which is associated with poor response to ICI therapy in metastatic RCC.[23] Associations between HiTME subtypes and ccRCC-associated genes indicated that *BAP1*, *PBRM1*, and *NF2* mutations were more prevalent in immune-enriched (IE and IE/M), V, and F HiTMEs, respectively (Figure S3A).

Comparative analysis of ccRCC HiTMEs and existing classifications

HiTME classifications were compared with published molecular subtypes: Clinical Proteomic Tumor Analysis Consortium (CPTAC),[25,26] IMmotion151,[12,14] and clear cell type A/B

(E) Heatmap of FGES and mean cytokine expression in cellular subpopulations in harmonized scRNA-seq data (n = 259,441 cells) from three public ccRCC cohorts.[18–20]

(F) Cell type proportions of WU-RCC ccRCC samples from Kassandra[21] deconvolution. Samples correspond with (D).

(G) Expression of $PDL1^+$ immune cells by IHC (n = 157), *IFNG* (n = 156), cytokine FGES from Mihecheeva et al. (*CCL4*, *CCL5*, *CXCL1*, *CXCL13*, *CD274*, and *TNFSF13B*; n = 156),[22] effector T cell FGES (n = 156), and angiogenesis FGES (n = 156) among Rs and NRs treated with ICIs and TKIs and untreated WU-RCC ccRCC patients. Mann–Whitney U test.

p value symbols are as follows: –, >0.05; *, <0.05, **, <0.01, ***, <0.001. For boxplots, the upper whisker indicates the maximum value or 75th percentile +1.5 IQR; the lower whisker indicates the minimum value or 25th percentile −1.5 IQR.

IHC, immunohistochemistry; RECIST, Response Evaluation Criteria in Solid Tumors; CR, complete response; PR, partial response; SD: stable disease; PD: progressive disease.

See also Figure S1; Tables S1 and S4.

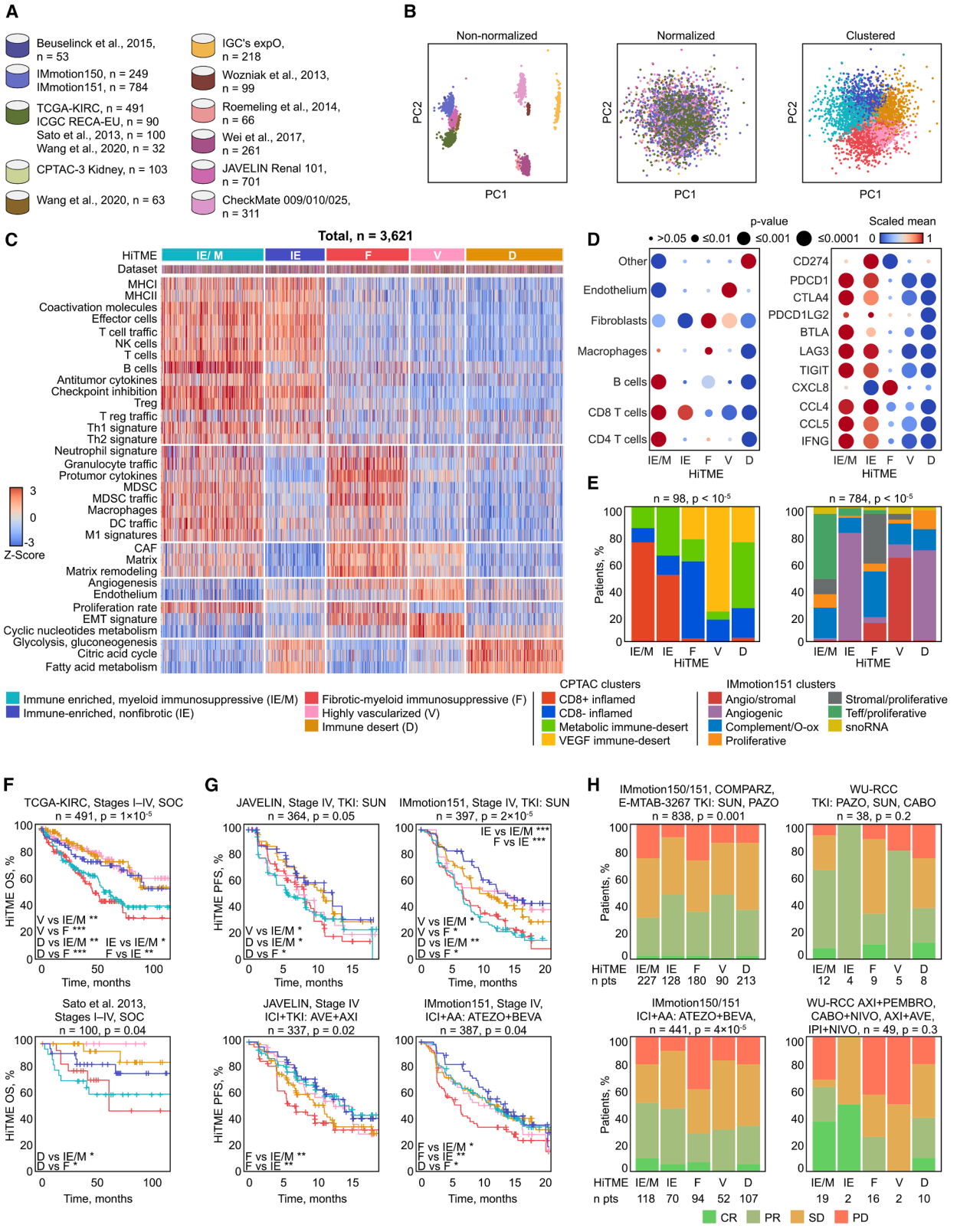

(legend on next page)

(ccA/ccB)[35] (Figures 2E and S3B). The HiTME classification exhibited the greatest degree of overlap with CPTAC signatures. A significant portion of the CPTAC CD8$^+$ inflamed samples were categorized into immune-enriched (IE/M and IE) subtypes (Figure 2E). Similarly, the majority of CPTAC CD8$^-$ inflamed samples were classified as subtype F, while a substantial portion of CPTAC VEGF/immune-desert samples were grouped as subtype V. CPTAC metabolic-immune desert samples primarily overlapped with subtype D. ccB samples were associated with fibrotic IE/M and F HiTMEs (Figure S3B). In contrast, IMmotion151 subtypes were more heterogeneously distributed (Figure 2E). Still, many IMmotion151 Teff/proliferative samples were classified as subtype IE/M, and a high proportion of Angio/Stromal samples were assigned to subtype V. Interestingly, IMmotion151 angiogenic samples were primarily grouped into subtypes IE and D. The IMmotion151 complement/Ω-Ox subtype was not reproducible, with distribution across all five HiTMEs. Survival analysis revealed that the HiTME subtypes were strongly associated with prognosis of various treatments in all studied datasets (Figures 2F and 2G). The Cancer Genome Atlas Kidney Renal Clear Cell Carcinoma (TCGA-KIRC)[27,28] and Sato et al.[29,30] cohort analysis demonstrated that fibrotic (IE/M and F) HiTMEs had the worst overall survival (OS) (Figure 2F). Consistent with these findings, stage III–IV ccRCC samples had higher proportions of fibrotic IE/M and F HiTMEs compared to early stages (Figure S3C). Survival analysis of the TCGA-KIRC cohort (n = 491; Figure S3D) revealed that V and D HiTMEs had worse hazard ratios (HRs) than subtype F, independent of stage. These findings suggest that the HiTMEs can, in part, predict survival in this cohort. Additionally, subtypes IE/M and F were more prevalent among patients with poor IMDC (International Metastatic RCC Database Consortium) scores (Figure S3E). Conversely, higher proportions of subtypes V, IE, and D were observed among patients with favorable IMDC scores.

Three experienced pathologists examined sarcomatoid and rhabdoid features for all cases from the CPTAC-ccRCC and TCGA-KIRC cohorts with available histological images. Cases were classified as sarcomatoid, rhabdoid, or non-sarcomatoid based on the World Health Organization/International Society of Urological Pathology criteria.[36] The sarcomatoid samples were associated more frequently with subtypes IE/M, IE, and F (Figure S3F). These results are consistent with previous findings[10] showing sarcomatoid samples with higher immune cell proportions and proliferation rates. Rhabdoid samples were also associated with subtypes IE/M and F (Figure S3G).

Association of HiTMEs with treatment response

To study relationships between HiTMEs and treatment response, we analyzed stage IV patients from IMmotion151[10,14] and JAVELIN (Figure 2G).[6] Strikingly, patients with fibrotic subtypes F and IE/M had shorter progression-free survival (PFS) in the sunitinib arm of both trials, whereas patients with immune-enriched subtypes IE/M and IE benefited more from combinations of anti-PDL1 ICIs and AAs compared to patients with subtype F.

Treatment response was further evaluated on TKI-treated patients from IMmotion150 (n = 79),[9,13] IMmotion151 (n = 365),[10,14] COMPARZ (n = 341),[31,32] and E-MTAB-3267 (n = 53)[33,34]; IE and V HiTMEs contained the highest proportion of TKI Rs (p = 0.001; Figures 2H and S3H). ICI response was also analyzed on IMmotion150 (n = 79)[9] and IMmotion151 (n = 362)[10] samples treated with ICIs+AAs. Subtypes IE and IE/M had increased proportions of ICI Rs ($p = 4 \times 10^{-5}$; Figures 2H, S3H, and S3I), while subtype F had the largest proportion of ICI NRs. In line with survival analysis, subtype IE/M exhibited the largest decrease in CRs with TKIs only (Figure 2H). Though statistically nonsignificant, WU-RCC IE/M and IE samples appeared likely to respond to ICIs (p = 0.3), while V and IE patients appeared responsive to TKIs (p = 0.2; Figure 2H).

HiTME subtype validation with MxIF

MxIF was leveraged to spatially characterize ccRCC and further validate the HiTMEs on a subset of patients (n = 34; Table S5; Figures 3A and S4). A custom ccRCC antibody panel (n = 19 markers; STAR Methods) was used for the spatial assessment of epithelial cell structures (CAIX$^+$, PanCK$^+$) and immune cell profiling, including CD68$^+$ or CD206$^+$ myeloid and immune subpopulations (Figure 3A). Normalized mean expression levels of markers in segmented cells were used to define cell populations within MxIF micrographs (Figures 3B and S5A, STAR Methods). Mask-based analysis was used to characterize myeloid, stromal,

Figure 2. Development of ccRCC HiTME subtypes

(A) Fourteen ccRCC cohorts were grouped into 11 batches to generate the harmonized transcriptomic database (n = 3,621).

(B) RNA-seq expression normalization across cohorts (n = 3,621). Principal component analyses, left to right: gene expression matrix, 33 normalized FGES scores,[15] 33 normalized FGES scores by HiTME subtype. Dots: individual samples; colors: batches from (A) (left, middle) and HiTME subtypes from (C) (right).

(C) Heatmap of 3,621 ccRCC samples clustered into five HiTME subtypes. Colors: datasets correspond with batches in (A).

(D) Bubble plot of differentially expressed features in each HiTME. Left: percentage of deconvolved cell types; right: gene expression. Bubble size: p values derived from Mann–Whitney U tests; color: scaled mean.

(E) Comparison of HiTMEs with CPTAC[25,26] and IMmotion151[12] ccRCC classifications. Barplots represent distribution of CPTAC or IMmotion151 clusters within HiTMEs.

(F) Kaplan–Meier plots with overall survival (OS) for patients treated with standard of care (SOC) in The Cancer Genome Atlas Kidney Renal Clear Cell Carcinoma (TCGA-KIRC)[27,28] and Sato et al.[29,30] datasets stratified by HiTME. Pairwise log rank test (p values within plot); multivariate log rank test (p values in plot titles).

(G) Kaplan–Meier plots of progression-free survival (PFS) for stage IV patients treated with TKIs and TKIs+ICIs from JAVELIN Renal 101 and IMmotion151. Samples were stratified by HiTME. Pairwise log rank test (p values within the plot); multivariate log rank test (p value in plot titles).

(H) Distribution of RECIST response across HiTME subtypes in patients with ccRCC. Top: TKI-treated samples from IMmotion150 (n = 79), IMmotion151 (n = 365), COMPARZ[31,32] (n = 341), E-MTAB-3267[33,34] (n = 53), and WU-RCC (n = 38) cohorts. Bottom: IMmotion150 (n = 83) and IMmotion151 (n = 362) ICI+AA-treated samples. WU-RCC ICI- and ICI+TKI-treated samples (n = 49, bottom right). Chi-square test.

p values are listed in either the plots or plot titles if applicable, as indicated in the legends.

ICI, immune checkpoint inhibitor; TKI, tyrosine kinase inhibitor; RECIST, Response Evaluation Criteria in Solid Tumors; CR, complete response; PR, partial response; SD, stable disease; PD, progressive disease.

See also Figures S2 and S3; Tables S4 and S7.

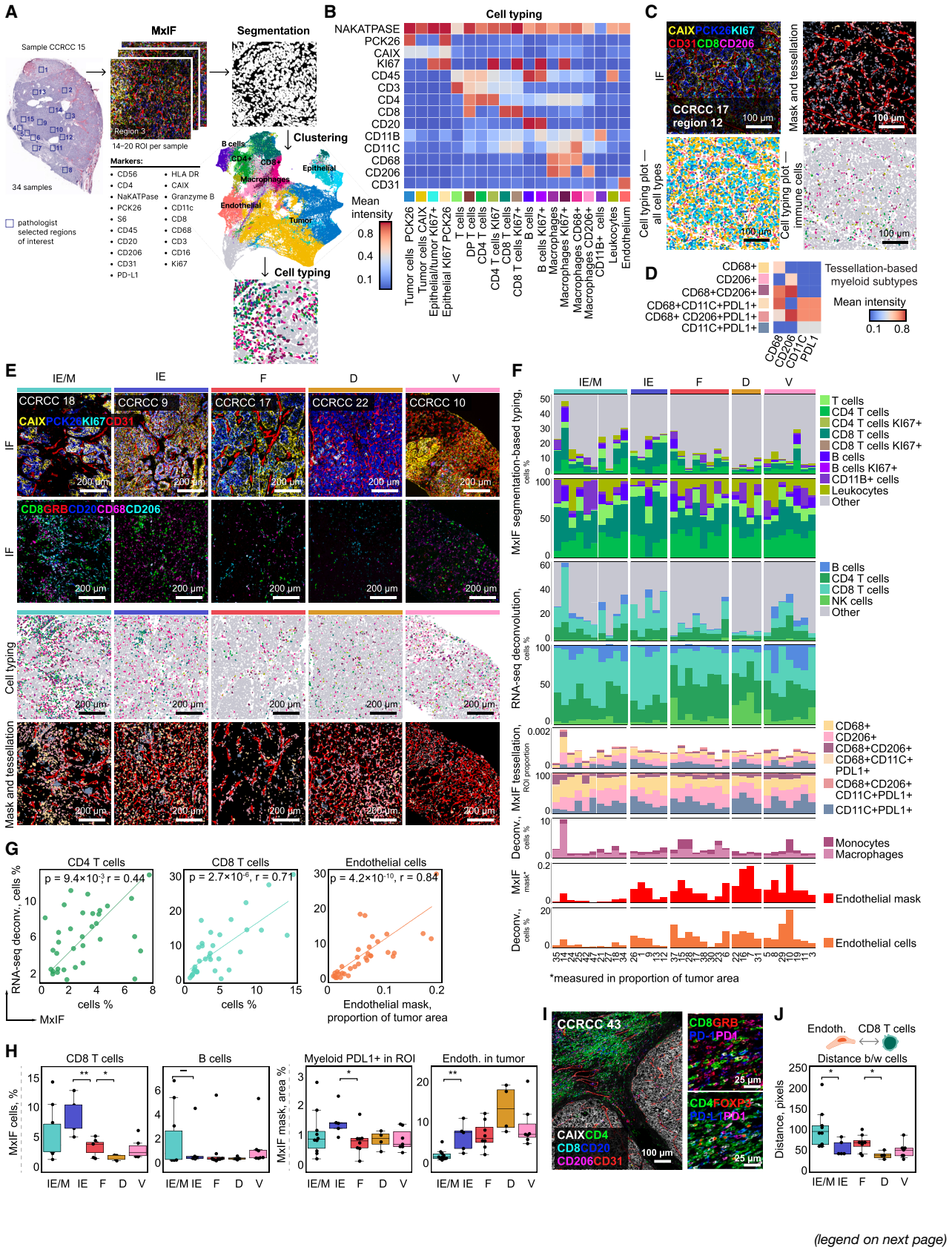

(legend on next page)

and endothelial cells (Figures 3C and 3D, STAR Methods).[37] After cell segmentation, clustering, and phenotyping, the MxIF images were visually similar to the corresponding HiTME subtypes (Figures 3E and S5B). The IE/M and F HiTMEs had fewer developed vascular structures, while the V HiTME had overdeveloped, branched vascular networks (Figure 3E). Cell types from RNA-seq deconvolution ($CD4^+$ T cells, $CD8^+$ T cells, B cells, macrophages, and endothelial cells) were compared to MxIF-based quantification, $CD68^+$ and $CD206^+$ tessellation masks, and endothelial tumor area (Figure 3F). MxIF and RNA-seq showed that IE and IE/M HiTMEs had the highest proportions of immune cells, including T and NK cells, while IE/M and F HiTMEs contained high proportions of myeloid cells. Correlations were measured for MxIF and RNA-seq identification of $CD4^+$ T cells ($r = 0.44$, $p = 0.0094$), $CD8^+$ T cells ($r = 0.71$, $p = 2.7 \times 10^{-6}$), B cells ($r = 0.49$, $p = 0.0035$), macrophages ($r = 0.36$, $p = 0.039$), and endothelium ($r = 0.84$, $p = 4.2 \times 10^{-10}$; Figures 3G and S5C). MxIF revealed that the IE and IE/M HiTMEs contained the highest levels of $CD8^+$ T and $PDL1^+$ myeloid cells, while endothelial cells were highest in the V, F, and D HiTMEs. Consistent with high B cell content in IE/M HiTMEs, IE/M MxIF images frequently exhibited tertiary lymphoid structures (Figures 3H and S5D–S5F), a marker associated with ICI response.[38]

Spatial analysis showed that IE samples contained strong immune cell infiltration near the tumor-stromal border, suggesting that immune cells migrated to the tumor (Figure 3I). Intriguingly, the IE/M HiTME had the greatest mean distances between endothelial cells and $CD8^+$ T cells or macrophages, potentially indicative of active immune cell migration from the vascular system into the tumor (Figures 3J and S5G).

Characterization of spatial cellular communities within each HiTME subtype

Spatial cell-to-cell interactions in WU-RCC samples were examined using graph-based cellular communities (Figure 4A, STAR Methods). This analysis defined 15 cellular communities with distinct cell type proportions (Figures 4B and S5H), representing malignant (E1–E4/I), vasculature-related (E5/V, V1, and V2), inflammatory (I1–I3), T cell-enriched (T1), B cell-enriched (B1), and myeloid cell-enriched (M1, M2, and CD11b) communities (Figures 4B, 4C, and S5I). Each HiTME contained the expected cell types and proximity communities associated with angiogenic, myeloid, immune-enriched, and/or malignant features (Figure 4D). For example, E1 was associated with $KI67^+$ tumor cells, while E2 was associated with nonproliferative tumor cells (Figure 4B). IE/M samples were enriched with community I2 ($CD68^+$-enriched; Figure 4E). Similarly, community E5/V was abundant in D samples. Conversely, communities E4/I, V1, and E5/V were minimal in subtype IE/M (Figure 4E). For each sample, community proportions in the intratumoral and tumor-stroma border regions of interest (ROIs) were determined (Figures 4D and 4F). Generally, communities E1, E3, and E5/V were prevalent in intratumoral ROIs, while communities V2, CD11B, and M2 were concentrated at the tumor-stroma border (Figure 4G). The vascularized V1 community significantly decreased with disease stage (Figure 4H), supporting RNA-seq-derived findings showing a decreased proportion of the V HiTMEs by stage (Figure S3C).

Robust genomic and transcriptomic relationships with immunotherapy response

Differential expression analysis was conducted with WU-RCC ($n = 49$), IMmotion150 ($n = 163$),[9,13] and IMmotion151 ($n = 362$)[12,14] to uncover transcriptomic biomarkers for ICI Rs and NRs. Genes selected using differential expression analysis were analyzed for pathway enrichment (Table S6). Strong myogenesis FGES scores trended with ICI resistance (Figure S5I), concurring with previous findings on immunotherapy nonresponse in melanoma.[39] Increased ECM-associated FGES expression was associated with ICI response (Figure S5J).

Analyzing genomic alterations and ICI response, we found that no patients with mutations in antigen presentation (AP) genes

Figure 3. Validation of ccRCC HiTME subtypes with MxIF

(A) MxIF pipeline. Left: representative H&E image of resected kidney cancer for patient CCRCC 15; rectangles mark the 15 regions of interest (ROIs). Middle: regions of interest (ROIs) from an MxIF image for the sample. Right: cell segmentation, a t-distributed stochastic neighbor embedding (t-SNE) plot of cell clusters derived from MxIF analysis, and cell typing.

(B) Heatmap of normalized mean marker expression of segmented cell populations from WU-RCC MxIF images ($n = 34$ patients).

(C) Representative MxIF processing. MxIF image with CAIX (yellow), PCK26 (blue), KI67 (cyan), CD31 (red), CD8 (green), CD206 (magenta; top left). Tessellation masks of six myeloid populations and blood vessels (CD31; top right). Cell typing plot for all cell populations (bottom left) and immune cells (bottom right). Scale bars: 100 μm.

(D) Heatmap of normalized mean marker expression in six myeloid clusters based on tessellation masks of selected protein markers.

(E) Representative MxIF images for the corresponding HiTME subtypes. Top row: immunofluorescence (IF) for CAIX, PCK26, KI67, and CD31. Second row: IF for CD8, granzyme B (GRB), CD20, CD68, and CD206. Third row: cell types based on (B). Bottom: endothelium mask (red) and tessellation based on (D). Scale bars: 200 μm.

(F) TME landscape derived from MxIF and RNA-seq. Cell typing plots from segmentation and tessellation masks with corresponding Kassandra[21] cell deconvolution ($n = 34$). Samples were grouped by HiTME subtype.

(G) Scatterplots with percentages of $CD4^+$ T, $CD8^+$ T, and endothelial cells from bulk RNA-seq and cell percentages or masks from MxIF. Correlation coefficients and p values (listed in plots) were derived from two-sided Spearman rank test.

(H) Boxplots with distributions of $CD8^+$ T, B, myeloid PDL1, and endothelial cells from MxIF samples ($n = 34$) across HiTMEs.

(I) Representative MxIF image of an IE/M HiTME sample with high immune infiltration at the tumor-stromal border; T cells are positive for GRB and PD1. Scale bars: left image, 100 μm; right images, 25 and 25 μm.

(J) Boxplot showing the association of the distance between endothelial and $CD8^+$ T cells across HiTMEs.

p value symbols are as follows: –, >0.05, *, <0.05, **, <0.01, ***, <0.001. For boxplots, the upper whisker indicates the maximum value or 75th percentile +1.5 IQR; the lower whisker indicates the minimum value or 25th percentile −1.5 IQR.

See also Figures S4 and S5; Table S5.

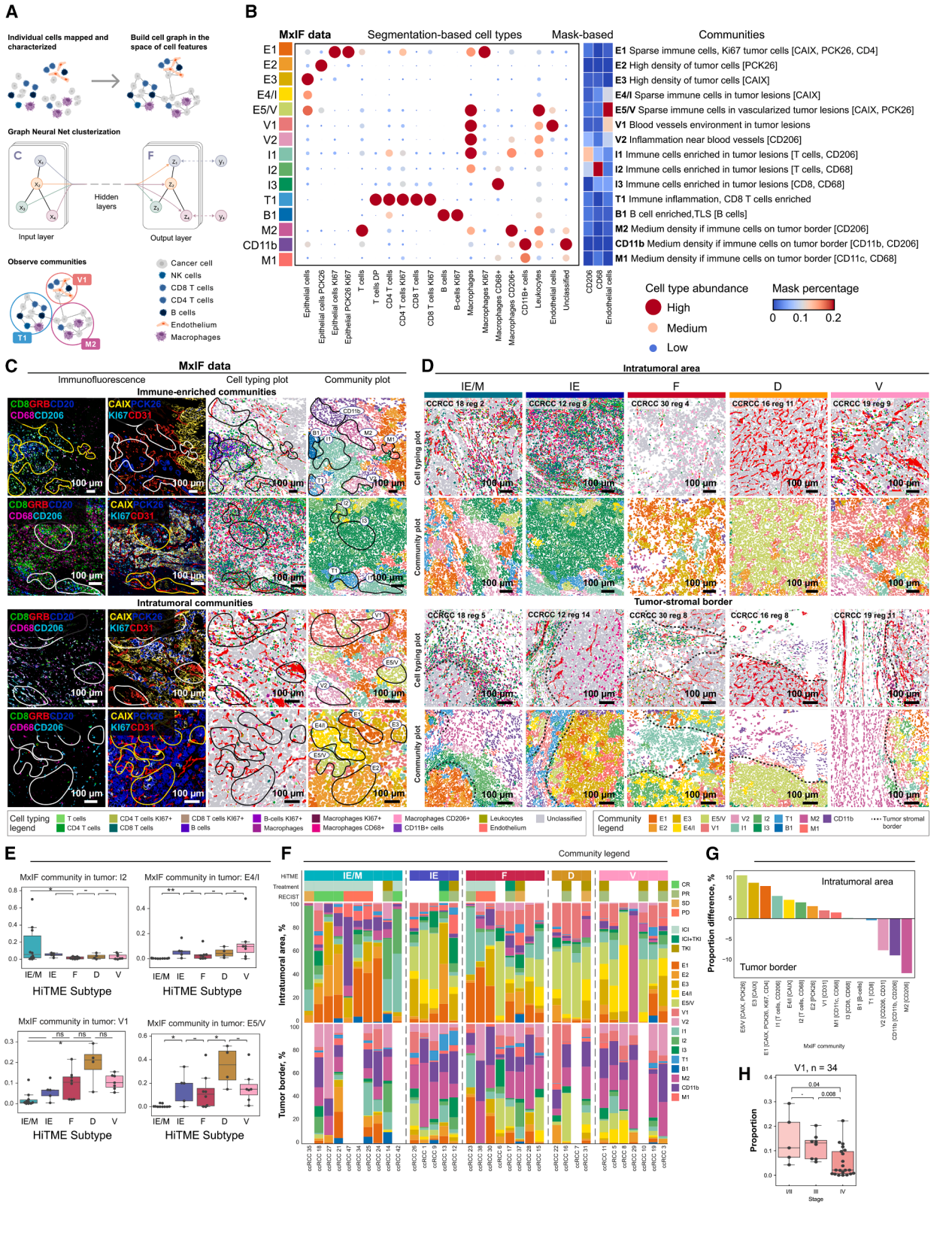

(legend on next page)

exhibited CR to ICI or ICI+TKI (Figure S5K). Moreover, 15 out of 16 patients with mTOR-activating mutations were resistant to ICI regimens (Figure S5L). Although rare, AP gene and *MTOR* mutations were strongly associated with ICI and ICI+TKI nonresponse. Our findings indicated patients with these mutations or strong myogenesis FGESs as unlikely to respond to ICIs. These patients were marked as "molecular ICI NRs."

AI-guided modeling of ICI and TKI response

An ML-based ICI response prediction model was developed using ICI-treated ccRCC training (n = 214 samples; IMmotion151, IMmotion150, and CheckMate 009/010/025)[7,9,12–14] and validation (n = 430 samples; JAVELIN, WU-RCC, and E-MTAB-3218) cohorts (Figures 5A and S6A; Table S3, STAR Methods). Previously defined transcriptomic parameters—similarity to subtypes IE and F; *PDCD1* (PD1) and *CD274* (PDL1) expression; and angiogenesis, proliferation, and ECM-associated FGESs—were used. All molecular ICI NRs, as defined previously, were assigned an ICI responder score of 0 and were removed from training. The gradient boosting ML model was first trained to distinguish CR from PD (Figures 5B and S6B) and then validated by grouping patients with ccRCC by their ICI responder scores (Figures 5C and S6C). For model output, the responder scores ranged from 0 (low response probability) to 1 (high response probability). ICI responder scores were divided into low (quartile [Q] 1), medium (Q2–Q3), or high (Q4) groups.

Patients with PR and SD had intermediate ICI responder scores (Figures 5D and S6B); therefore, they were excluded from the training set and included in validation. Kaplan–Meier analysis of IMmotion151 stratified by responder scores during model training revealed concordance with PFS (Figure 5E). ICI responder scores from training also discriminated CR and PR from PD (area under the receiver operating characteristic curve, ROC-AUC = 0.77, Figure 5F).

WU-RCC, JAVELIN, and E-MTAB-3218 were used for validation (Figures 5A and S6C). The proportions of Rs stratified by high, medium, and low ICI responder scores were statistically significant in WU-RCC (CR vs. PD, p = 0.04; CR vs. SD, p = 0.05; Figure 5G). Patients in the JAVELIN validation cohort with high responder scores had the longest PFS (p = 0.006, Figure 5H; ROC-AUC = 0.78; Figure 5I).

Samples from IMmotion151 and JAVELIN with high ICI responder scores had significantly lower HRs (IMmotion151 HR = −0.52, p = 0.003; JAVELIN HR = −0.55, p = 0.01) compared to previously published signatures and biomarkers (Figure 5J). Though nonsignificant, immune-inflamed signatures from IMmotion150 and JAVELIN[6,9] had decreased HRs, while high IMmotion150 myeloid signatures were associated with increased HRs. Expression of *CXCL8*, *CD274* (PDL1), and the JAVELIN Angio signature had no clear effect on HRs. These analyses suggest that our proposed AI-based ICI responder score was the only metric with consistent trends across cohorts.

ML-based algorithms were also used to generate a harmonized predictive model for TKI response. The model was trained on E-MTAB-3267[33,34] and IMmotion151[10] (n = 240 patients) and validated on WU-RCC,[16] JAVELIN,[6] IMmotion150,[9] and COMPARZ (n = 822 patients; Figures 5K and S7A; Table S3).[31,32] The final TKI model featured angiogenic, macrophage, and proliferation rate FGESs (Figures 5L and 5M). TKI responder scores were interpreted as low (<0.55), medium (0.55–0.80), and high (>0.80). During training, samples with SD had significantly lower TKI responder scores than CRs and PRs, and PD patients had the lowest TKI responder scores (Figures 5N and S7B). Similarly, high and low TKI responder scores from IMmotion151 training data correlated with the longest and shortest PFS, respectively (Figure 5O; ROC-AUC = 0.66; Figure 5P).

TKI responder scores were validated using the WU-RCC, JAVELIN, and COMPARZ ccRCC samples (Figures 5K and S7C). Collectively, Rs had significantly higher TKI responder scores than NRs (p = 0.0003), while PD samples had the lowest scores (p < 0.001; Figure 5Q). The proportions of Rs in the individual cohorts varied when samples were grouped by TKI responder scores (Figure S7C). JAVELIN patients with low TKI responder scores had the lowest PFS (Figure 5R). Overall, the TKI responder model effectively discriminated Rs from NRs (ROC-AUC = 0.74, Figure 5S).

The predictive value of the TKI responder scores was interpreted against relevant FGESs and previously published signatures from IMmotion151,[10,14] COMPARZ,[31,32] JAVELIN,[6] and E-MTAB-3267[33,34] (Figure 5T). Low TKI responder scores were significantly associated with high HRs in four cohorts, while high proliferation FGESs were associated with significantly higher HRs in only two cohorts. HRs associated with low JAVELIN and IMmotion150 Angio signatures were less significant than TKI responder scores. Although low JAVELIN and IMmotion150 Angio signatures performed better than most other

Figure 4. Spatial cellular communities within HiTME subtypes

(A) Proximity community clustering for identifying cell-cell interactions. Cellular interactions were graphed and clustered into 15 communities (STAR Methods; n = 34).

(B) Left: dotplot of relative cell type proportions identified in 15 proximity-based community clusters. Right: heatmap showing the proportion of myeloid masks in the proximity radius of the specified cell community. Each row denoted one community.

(C) MxIF-based segmented images, cell typing, and community plots representing different cell-cell interactions or cellular niches identified in proximity-based community clusters. Scale bars: 100 μm.

(D) Representative MxIF images of community composition across HiTMEs in intratumoral and tumor border regions. Scale bars: 100 μm.

(E) Boxplots of associations between HiTMEs and selected MxIF communities (n = 34). Mann–Whitney U test.

(F) Community composition within each sample grouped by HiTME.

(G) Proportion differences in MxIF communities in intratumoral and tumor border regions.

(H) Boxplot showing the association between the proportion of the V1 community in MxIF and disease stages (n = 34). Mann–Whitney U test.

p value symbols are as follows: –, >0.05, *, <0.05, **, <0.01, ***, <0.001. For boxplots, the upper whisker indicates the maximum value or 75th percentile +1.5 IQR; the lower whisker indicates the minimum value or 25th percentile −1.5 IQR.

See also Figure S5; Table S5.

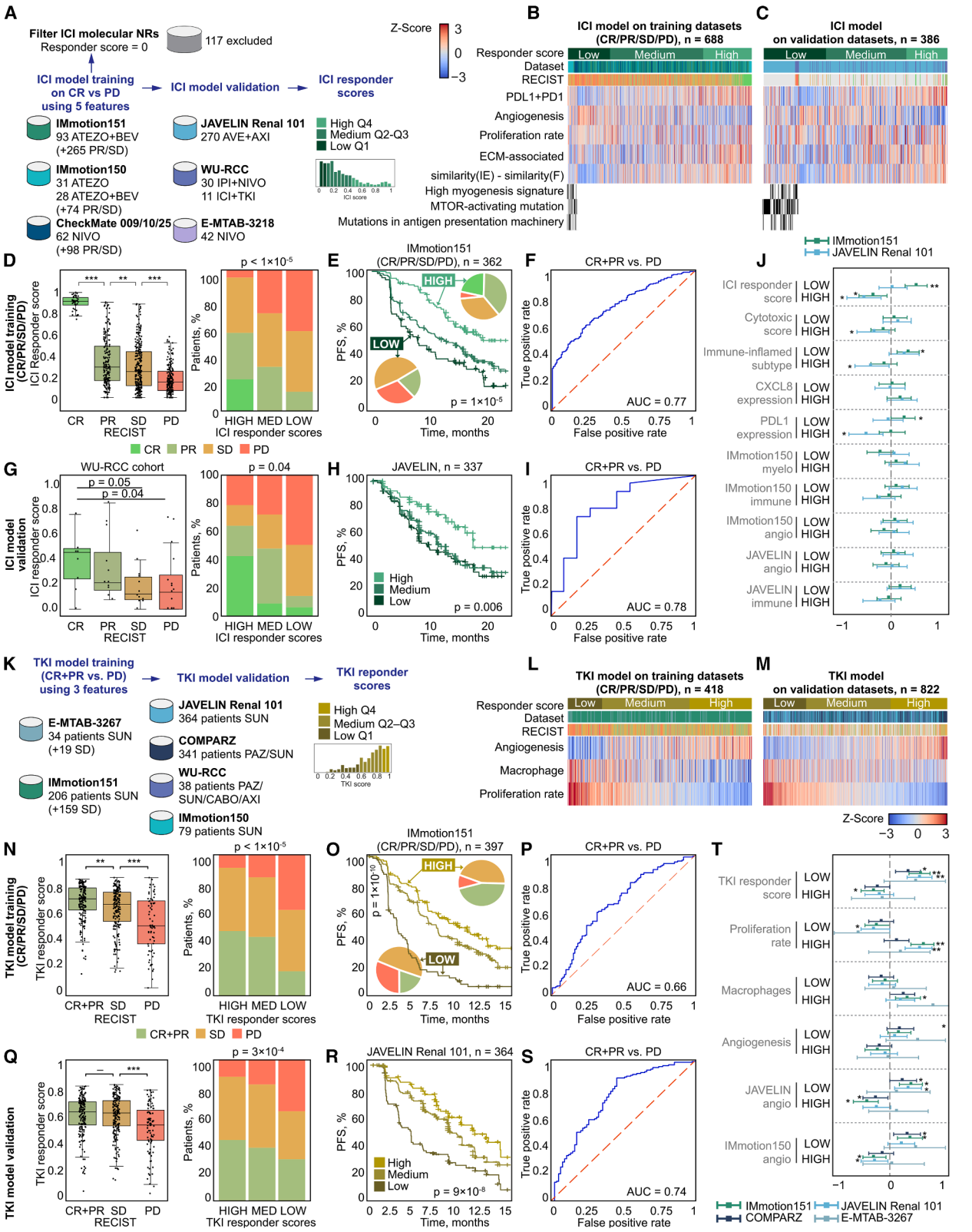

(legend on next page)

signatures (i.e., proliferation, macrophages, and angiogenesis), the low TKI responder score outperformed all available TKI prediction models across the analyzed datasets (Figure 5T).

Survival analysis (Figure S8) showed that ICI responder scores were not predictive for TKI-treated samples and vice versa (Figure S8A). Additional validation was performed on TCGA-KIRC data,[27] which contained no ICI-treated samples (Figure S8B). Consistent with the hypoxia-inducible factor (HIF)-based ccRCC pathogenesis, patients with lower TKI responder scores in TCGA-KIRC cohort were associated with worse OS and higher stages. ICI responder scores showed no association with OS or stage (Figure S8B).

Clinical applications of TKI and ICI responder scores

To assess the clinical value of our ICI and TKI responder scores, we assigned ccRCC samples from IMmotion151[10,12] patients treated with atezolizumab+bevacizumab versus sunitinib with TKI and ICI responder scores and PFS (Figure 6A). Samples with ICI-high/TKI-low scores exhibited a significant survival benefit from atezolizumab+bevacizumab compared to single-agent sunitinib (p = 0.0003). Patients with ICI-high scores accompanied by TKI-high (p = 0.03) or -medium (med) scores (p = 0.3) exhibited longer PFS when treated with bevacizumab +atezolizumab and were classified as ICI/ICI combination (combo)-preferred. Conversely, patients with ICI-low/TKI-med or ICI-med/TKI-high scores exhibited longer PFS when treated with sunitinib alone (p = 0.02 and p = 0.06, respectively) and were classified as TKI-preferred. Similar trends were observed using JAVELIN samples, but the results were weaker, potentially because of the absence of *MTOR* and AP mutation data (Figure S8A).

Comprising 2% of the cohort, ICI-low/TKI-low patients responded poorly to both AA and ICI treatments with the worst survival for both treatment arms. These TMEs were characterized by strong myogenesis signatures (Figure 6B); increased macrophages, CAFs, protumor cytokines, and proliferation signatures; and low vascularization, implicating an immunosuppressed, protumor microenvironment (Figures 6C and S8E). Alternative treatment options are needed for this molecularly distinct patient subgroup.

ICI and TKI responder scores were significantly associated with but not determined by the mutational profiles of key ccRCC genes. Of note, ICI-low, TKI-high, and TKI-low samples harbored more *MTOR*, *PBRM1*, and *BAP1* mutations, respectively (Figure 6D), all genomic features previously associated with therapy response.[6,12]

Using the IMmotion151[10,12] and JAVELIN[6] cohorts, our decision-tree model classified 56% of patients as ICI/ICI combo-preferred, 41% as TKI-preferred, and 3% as non-responsive to either (Figures 6E and S8F). Survival analysis showed that

Figure 5. ICI and TKI responder score training and validation

(A) Training and validation scheme for the ICI response model.[6,7,9–14,33,34] The model was trained on CR versus PD. ICI molecular nonresponders (NRs; n = 117) were filtered during training.

(B) Heatmap of features used in the ICI response model on training data grouped by ICI responder score.

(C) Heatmap of features used in the ICI response model on validation data grouped by ICI responder score.

(D) Left: ICI responder scores for training samples (n = 688) grouped by RECIST outcome. Mann–Whitney U test. Right: proportions of RECIST outcomes from training data grouped by ICI responder score. Chi-square test.

(E) PFS of ICI-treated patients from IMmotion151 training data (n = 362) grouped by ICI responder score. Pie charts show RECIST distribution for high and low ICI responder groups. Multivariate log rank test; p = 0.00001.

(F) ICI responder score ROC-AUC curve for discrimination between CR+PR and PD in ICI-treated samples from training data.

(G) Left: ICI responder scores for validation samples (n = 49) grouped by RECIST outcome. Mann–Whitney U test. Right: proportions of RECIST outcomes grouped by ICI responder scores on the validation data. Chi-square test.

(H) PFS of ICI-treated patients within the JAVELIN Renal 101 validation data (n = 337) grouped by responder score. Multivariate log rank test; p = 0.006.

(I) ICI responder score ROC-AUC curve for discrimination between CR+PR and PD in ICI-treated samples from WU-RCC validation data.

(J) Cox proportional hazards models for ICI responder scores, cytotoxic scores, immune-inflamed subtype, *CXCL8* expression, *CD274* (PDL1) expression, IMmotion150 (myelo, immune, angio) signatures,[9] and JAVELIN Renal 101 (angio and immune) signatures[6] on IMmotion151 training and JAVELIN Renal 101 validation datasets.

(K) Training and validation schema for the TKI response model. The model was trained on CR+PR versus PD.

(L) Heatmap of features utilized in the TKI therapy response model on training samples grouped by TKI responder score.

(M) Heatmap of features utilized in the TKI therapy response model on validation samples grouped by TKI responder score.

(N) Left: TKI responder scores for training samples (n = 418) grouped by RECIST outcome. Mann–Whitney U test. Right: proportions of RECIST outcomes on the training samples grouped by TKI responder scores. Chi-square test.

(O) PFS of TKI-treated patients within the IMmotion151 training data (n = 397) grouped by TKI responder scores. Pie charts show RECIST distribution for high and low ICI responder groups. Multivariate log rank test.

(P) TKI responder score ROC-AUC curve for discrimination between CR+PR and PD in TKI-treated training samples.

(Q) Left: TKI responder scores for validation samples (n = 822) grouped by RECIST outcome. Mann–Whitney U test. Right: proportions of RECIST outcomes grouped by TKI responder score on validation data. Chi-square test.

(R) PFS of TKI-treated patients from JAVELIN Renal 101 validation data (n = 364) grouped by ICI responder score. Multivariate log rank test.

(S) TKI responder score ROC-AUC curve for discrimination between CR+PR and PD in TKI-treated validation samples.

(T) Cox proportional hazards models for TKI responder scores, proliferation rate, macrophages, angiogenesis, JAVELIN Renal 101,[6] and IMmotion150[9] Angio signatures on IMmotion151 and E-MTAB-3267 training and JAVELIN Renal 101 and COMPARZ validation datasets.

p value symbols are as follows: –, >0.05, *, <0.05, **, <0.01, ***, <0.001. For boxplots, the upper whisker indicates the maximum value or 75th percentile +1.5 IQR; the lower whisker indicates the minimum value or 25th percentile −1.5 IQR.

ICI, immune checkpoint inhibitors; TKI, tyrosine kinase inhibitors; ROC-AUC, area under the receiver operating characteristic curve; PSF, progression-free survival; RECIST, Response Evaluation Criteria in Solid Tumors; CR, complete response; PR, partial response; SD, stable disease; PD, progressive disease.

See also Figures S6 and S7; Tables S4 and S6.

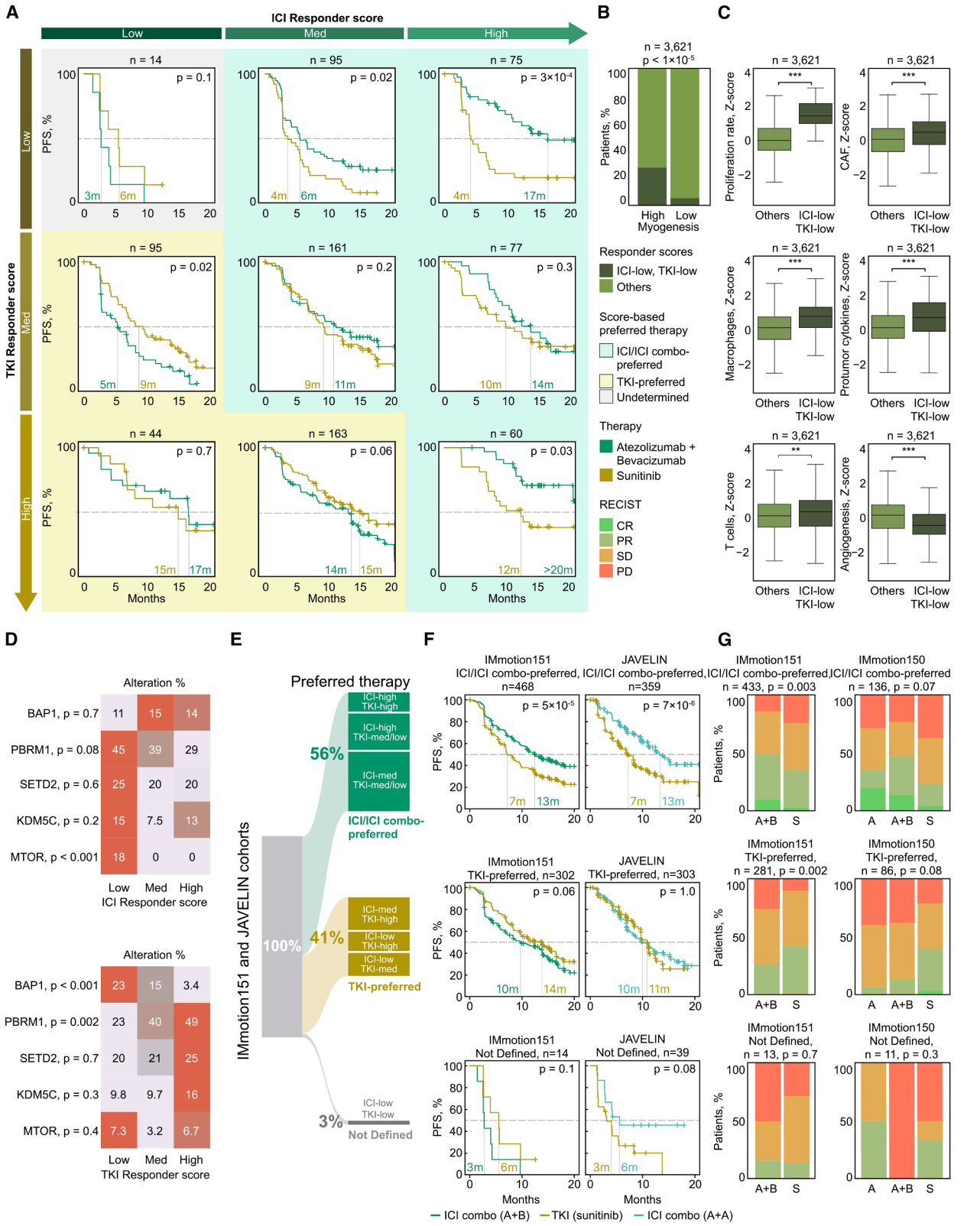

(legend on next page)

ICI/ICI combo-preferred patients had increased PFS when treated with atezolizumab plus bevacizumab compared to sunitinib (IMmotion151, $p = 0.00005$), and with avelumab plus axitinib compared to sunitinib (JAVELIN, $p = 0.000007$, Figure 6F). Longer PFS was also observed in TKI-preferred patients receiving sunitinib (median PFS = 14 months) compared to those receiving bevacizumab+atezolizumab (median PFS = 10 months, $p = 0.06$). Expectedly, no differences were observed in TKI-preferred patients treated with TKI-containing therapies avelumab plus axitinib or sunitinib ($p = 1.0$; Figure 6G).

Intratumoral spatial cellular communities associated with HiTME subtypes and ICI/TKI responder scores

Correlations among individual MxIF-based communities and HiTME subtypes, treatment response, and ICI/TKI responder scores were evaluated to determine underlying spatial factors. Intriguingly, five ICI NRs had increased community E1, while three CRs had higher E2 (Figure 7A). Significant relationships were confirmed between community I1 ($CD206^+$-enriched) and subtype F ($p < 0.05$), communities I2 ($CD68^+$-enriched) and M1 and subtype IE/M ($p < 0.05$), and community V1 and TKI responder scores ($p < 0.001$; Figures 7B and S8G).

MxIF community analysis further improved next-generation sequencing-based stratification of Rs and NRs (Figure 7C). The multimodal approach more effectively distinguished CR from PD on ICI-treated samples ($n = 13$). After the addition, the model identified only one PD sample, which was originally incorrectly assigned a high ICI responder score (0.74). This highlights the potential of multimodal biomarkers for patient selection and therapeutic decision-making in immunotherapy trial design and optimization.

Cellular communities defined by cytokine programs

Cytokines were further investigated due to their regulatory role in the tumor-immune ecosystem, tissue architecture, and different types of immune inflammation.[14,30] We previously showed that cytokines affect ccRCC outcomes and that only specific types of inflammation relate to immunotherapy response.[14] Hierarchical clustering correlation coefficients between cytokine and chemokine gene expression and MxIF-defined cellular communities revealed at least three distinct groups of cytokines coinciding with different types of immune inflammation and corresponding spatial communities (Figure 7D). scRNA-seq was used to estimate which cell types produced these cytokines and chemokines (Figure 7E).

Group 1 consisted of cytotoxic and aggressive inflammatory cytokines (*CXCL13*, *IFNG*, *CXCL9*, *CCL5*, *CXCL11*, *CXCL10*, *IL15*, and *CCL4*) mostly produced by myeloid and T cells for immune cell tissue trafficking (Figures 7D and 7E).[22] Expression of these cytokines was associated with communities M1, T1, B1, and I2, as well as abundant T cells and antigen-presenting cells (APCs). Moreover, Group 1 cytokines strongly correlated with ICI responder scores. Corresponding single-cell RNA analysis elucidated the cell populations involved in the production of specific cytokines (Figures 7E and 7F). $CD8^+$ T and NK cells were primary producers of *CCL5* (Figure 7F), while macrophages produced traffic-associated cytokines.

Group 2 consisted of myeloid-associated cytokines (*MMP14*, *CCL18*, *CCL20*, *IL6*, and *CXCL8*) produced by macrophages and fibroblasts (Figure 7D). Thus, their elevated expression could be associated with chronic inflammation resulting in immune suppression, favoring EMT and metastasis. Group 2 cytokines overlapped with subtype F and was associated with $CD206^+$ TAM-enriched communities (I1, M2, CD11b, and V2).

Group 3 contained angiogenesis-associated cytokines (*EPAS1*, *VEGFA*, *CXCL12*, *PDGFA/B*, *TGFB2/3*, *IL33*, and *HIF1A*) commonly produced by stromal cells, endothelial cells, and TAMs (Figures 7D–7F). *EPAS1* was primarily produced by endothelial cells (Figure 7F). This vascular and hypoxia-associated[40] group strongly correlated with TKI responder scores, subtypes D and V, and communities V1, E4/I, and E5/V, which were enriched in tumor and endothelial cells. These cytokines marked hypoxic regions with fibrosis, high angiogenesis, and activated endothelium with poor infiltration.

DISCUSSION

Despite advancements in molecular classifications and precision medicine, single biomarkers used to strategize ccRCC treatment have not been effective in predicting treatment response. Our analysis failed to uncover significant correlations between previously reported biomarkers or gene signatures and

Figure 6. An integrated predictive decision-tree model for ICI and TKI response

(A) Kaplan–Meier plots with PFS for patients from IMmotion151 treated with sunitinib (yellow) or atezolizumab+bevacizumab (green). Samples were grouped by ICI (*x* axis) and TKI (*y* axis) responder scores. Log rank test.

(B) Proportion of ICI- and TKI-low patients ($n = 3,621$) with high or low myogenesis FGES scores compared to all others. Chi-squared test.

(C) Proliferation rate, cancer-associated fibroblast (CAF), macrophage, protumor cytokine, T cell, and angiogenesis FGES *Z* scores in patients ($n = 3,621$) with ICI- and TKI-low scores compared to all others.

(D) Heatmaps illustrating percentages of *BAP1*, *PBRM1*, *SETD2*, *KDM5C*, and *MTOR* mutations within ICI- (top) and TKI (bottom)-low, -medium, and -high score groups. Chi-square test.

(E) Distribution of IMmotion151 ($n = 784$) and JAVELIN ($n = 701$) patients by preferred therapy: ICI alone or ICI combination (ICI/ICI combo-preferred), TKI alone (TKI-preferred), and not defined.

(F) Kaplan–Meier plots with PFS for patients from IMmotion151 (left) treated with sunitinib or atezolizumab plus bevacizumab (A+B) and JAVELIN (right) treated with sunitinib or avelumab plus axitinib (A+A) grouped by preferred therapy from the proposed ICI and TKI response models. Log rank test.

(G) Barplots with RECIST outcomes and therapy for IMmotion151 (left) and IMmotion150 (right) patients treated with sunitinib (S), atezolizumab (A), and atezolizumab plus bevacizumab (A+B). Samples were grouped into ICI/ICI combo- or TKI-preferred categories. Chi-square test.

p value symbols are as follows: –, >0.05, *, <0.05, **, <0.01, ***, <0.001. For boxplots, the upper whisker indicates the maximum value or 75th percentile +1.5 IQR; the lower whisker indicates the minimum value or 25th percentile −1.5 IQR.

ICI, immune checkpoint inhibitors; TKI, tyrosine kinase inhibitors; PSF, progression-free survival; RECIST, Response Evaluation Criteria in Solid Tumors.

See also Figure S8.

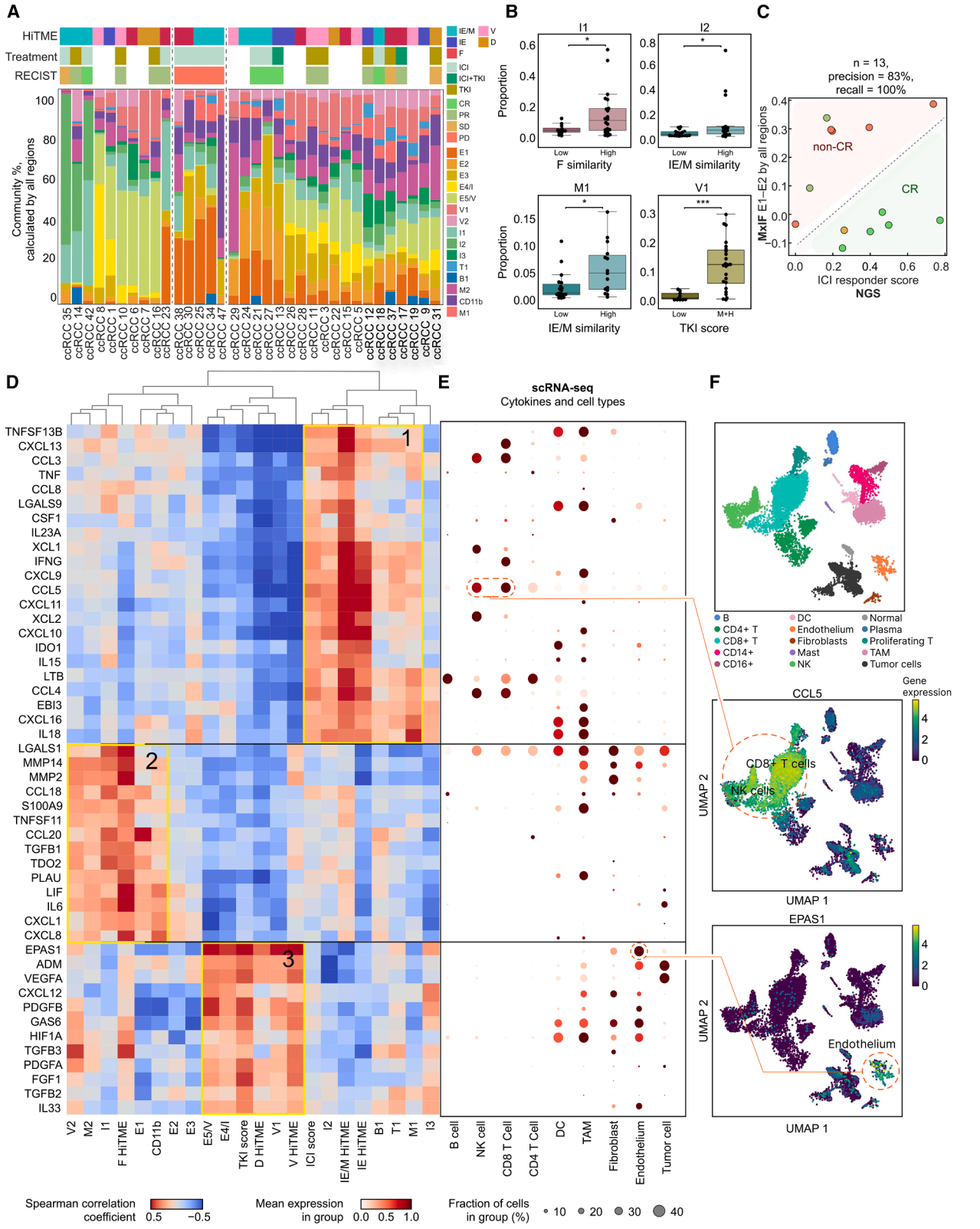

(legend on next page)

treatment response across independent cohorts,[41–49] underscoring the need for improved classification systems for estimating TKI and ICI treatment response. To address this need, we developed an algorithm encompassing multimodal harmonized biomarkers to stratify patients with ccRCC for ICI or TKI therapy.

Density-based clustering of 3,621 ccRCC samples from 14 public datasets in our harmonized transcriptomic database identified five distinct HiTMEs: IE, IE/M, F, D, and V. While subtypes IE and IE/M both contained high levels of immune infiltrate, IE/M additionally contained myeloid components and exhibited CAF and EMT FGESs associated with fibrosis. Increased survival among V samples may be due to enhanced vascularization and the expression of targetable receptor tyrosine kinases, while increased survival of IE samples may have resulted from the active immune TME.

Unlike previously described RCC signatures,[6,9–12] HiTME subtypes also accounted for myeloid FGESs, with fibrotic HiTME subtypes IE/M and F presenting the worst survival with standard of care (SOC). Subtype V expressed the highest levels of potentially druggable angiovascular targets. When treated with ICI +TKI combinations, subtypes IE and IE/M had the longest PFS and highest proportions of Rs, and subtype F had the shortest PFS and highest proportion of NRs. Interestingly, IE/M samples exhibited the most drastic decrease in PFS and proportion of CRs when treated with TKIs alone. CPTAC[25,26] and IMmotion151[10] signatures overlapped with corresponding HiTME subtypes, particularly among immune-enriched and angiogenic classifications.

Here, we used a multimodal AI-based approach to overcome the low predictive power of single biomarkers by combining several TME-associated biomarkers into ICI and TKI responder scores. This scoring system uncovered a small (3%), previously unidentified subset of patients unlikely to respond to either regimen. They had the lowest PFS and the worst prognosis and expressed high levels of macrophages, proliferation FGESs, CAFs, and protumor cytokines. Additional analysis of this group is warranted to uncover treatment options beyond the SOC. For instance, anti-proliferative and anti-fibrotic agents may benefit this group more than AA and ICI therapies.

Next, we identified cytokine groups regulating specific inflammation types. Group 1 cytokines were associated with ongoing antitumor immune response, strongly correlating with immune-enriched subtypes (IE and IE/M), ICI responder scores, and inflamed communities (I2, M1, T1, and B1) of B cells, T cells, and $CD68^+$ AP macrophages. Group 2 cytokines were largely immunosuppressive, produced by macrophages, and associated with fibrotic (IE/M and F) HiTMEs, which was corroborated by the presence of M2 and V2 communities enriched with $CD206^+$ myeloid cells. Group 3 cytokines were largely angiogenic factors related to hypoxia and fibrosis produced by endothelial and stromal cells, strongly correlating with cold immune subtypes (V and D), TKI responder scores, and malignant and vascularized communities (E5/V, E4/I, and V1). These cytokine signatures were associated with HiTMEs, tumor spatial architecture, and ICI and TKI response scores.

Similar to previous findings,[50] we uncovered two key transcription networks in ccRCC: angiogenesis and immune inflammation, underscoring the success of deploying TKIs and ICIs as mainstream therapeutic regimens. Contemporary trials established ICI+TKI combinations as preferred first-line treatment regimens for metastatic ccRCC regardless of risk category.

Our integrated multimodal scoring system most effectively stratified patients likely to benefit from TKI alone or ICI+TKI therapies. Validated on the largest ccRCC clinical dataset to date, our TKI and ICI responder scores can potentially identify patients most likely to respond to TKIs and TKIs+ICIs in the first-line setting. As new targeted therapies for RCC continue to emerge, we foresee our multimodal decision-tree model as a useful clinical tool for guiding personalized therapy.

Limitations of the study

Due to data limitations, our approach cannot stratify patients for evaluating the use of ICIs alone or anti-CTLA4+anti-PD1 combinations. In particular, data for SOC lenvatinib+pembrolizumab and nivolumab+cabozantinib combination are lacking.

The lack of patient data with clinical annotation and small sample sizes likely prevented us from assembling heterogeneous patient cohorts. Small sample sizes could also hamper our ability to adequately demonstrate statistical significance. Prospective clinical datasets are also lacking, thereby affecting our ability to test our models adequately.

Here, we utilized all accessible open-source datasets and our WU-RCC dataset with clinical annotation. The training and test cohorts may be skewed toward certain types of immunotherapies and targeted inhibitors. Our current approach

Figure 7. Analysis of ccRCC MxIF-based cellular communities

(A) Overview of community composition for each sample. Dotted lines mark a cluster of five patients with PD on ICI therapy.

(B) Boxplot demonstrating relationships among proportions of selected cellular communities with HiTME subtypes and TKI responder scores.

(C) Scatterplot of ICI-treated patients with ccRCC ($n = 13$) using the difference between E1 and E2 proximity communities and ICI responder scores. Patients were grouped by CR and non-CR.

(D) Heatmap of Pearson correlation coefficients describing relationships between transcriptomic cytokine expression and MxIF proximity communities, ICI and TKI responder scores, and HiTME subtype similarity. Hierarchical clustering of correlation coefficients resulted in three groups of cytokines (yellow boxes).

(E) Bubble plot with cell type-specific expression levels of cytokines from scRNA-seq dataset phs002065.v1.p1 ($n = 22{,}456$ cells). Bubble size is proportional to the fraction of cells expressing the cytokine.

(F) Uniform manifold approximation and projection (UMAP) of scRNA-seq analysis used in (E) with defined cell types. Additional UMAPs with *CCL5* and *EPAS1* expression across cell populations.

See also Figure S8.

p value symbols are as follows: –, >0.05, *, <0.05, **, <0.01, ***, <0.001. For boxplots, the upper whisker indicates the maximum value or 75th percentile +1.5 IQR; the lower whisker indicates the minimum value or 25th percentile −1.5 IQR.

ICI, immune checkpoint inhibitors; TKI, tyrosine kinase inhibitors; CR, complete response; PD, progressive disease.

involved combining the normalized gene signature data for all chosen datasets. While allowing us to minimize technical batch effects, this approach masked the biological features of each dataset. Therefore, HiTME subtypes will likely be more effective in comparing patients from cohorts with similar characteristics (Figure 2F). We performed spatial imaging and scRNA-seq for a limited subset of patient samples but still achieved statistically significant correlations. Given these limitations, more studies are warranted to refine and increase the functionality of our models.

RESOURCE AVAILABILITY

Lead contact

Requests for further information and resources should be directed to and will be fulfilled by the lead contact, Alexander Bagaev, PhD (aleksander.bagaev@bostongene.com).

Materials availability

This study did not generate new reagents.

Data and code availability

- Data availability: Data used in this study are available at https://doi.org/10.5281/zenodo.15296474. All published datasets are listed under "Deposited data" in the key resources table. Any additional information required to reanalyze the data reported in this paper is available from the lead contact upon request. Several datasets used in this study are not publicly available due to legal restrictions imposed by the data owners cited in the corresponding publications. Access to these data must be requested directly from the original data providers, following procedures similar to those we undertook during this study.
- Code availability: All software and algorithms used are listed in the key resources table. Additional code was deposited at https://zenodo.org/records/15608335.
- Other items: Any additional information required to reanalyze the data reported in this paper are available from the lead contact upon request.

ACKNOWLEDGMENTS

The results published here are in part based on data generated by TCGA Research Network: https://www.cancer.gov/tcga.

Data used in this publication were generated by the National Cancer Institute Clinical Proteomic Tumor Analysis Consortium (CPTAC).

This research was funded by BostonGene Corporation. We thank Anastasiya Troshina and Anna Kurilovich for figure design.

AUTHOR CONTRIBUTIONS

Conceptualization, N.F., E.C., J.J.H., and A.B.; methodology, A.R. and Y.L.; investigation, D.S., N.M., E.P., Y.L., A.R., I.G., G.K., K.P., S.M., A.T., V.S., M.B., A.V., and A.B.; formal analysis, D.S., N.M., E.P., Y.L., A.R., I.G., G.K., K.P., S.M., A.T., V.S., M.B., A.V., and A.B.; visualization, D.S., N.M., E.P., A.L., E.C., J.J.H., and A.B.; writing – original draft, D.S., N.M., E.P., G.K., A.L., E.C., J.J.H., and A.B.; writing – review and editing, D.S., N.M., E.P., Y.L., A.R., I.G., G.K., K.P., A.L., S.M., A.T., V.S., M.B., A.V., N.F., E.C., J.J.H., and A.B.; supervision, N.F., E.C., J.J.H., and A.B.

DECLARATION OF INTERESTS

J.J.H. received consulting fees and research funding from BostonGene Corporation. N.F. is the Chief Medical Officer, and A.B. is the Chief Product Officer of BostonGene Corporation. D.S., N.M., E.P., I.G., V.S., and A.B. have patents related to this work. All BostonGene-affiliated authors were employees thereof at the time the study was performed.

STAR★METHODS

Detailed methods are provided in the online version of this paper and include the following:

- KEY RESOURCES TABLE
- METHOD DETAILS
  - Experimental model and study participant details
  - Pathological examination
  - MxIF imaging
  - MxIF imaging data analysis
  - Next-generation sequencing (NGS)
  - DNA sequencing analysis: Alignment and variant calling
  - Mutations in *MTOR* and antigen presentation genes
  - RNA-seq processing
  - TME subtype identification
  - scRNA-seq analysis
  - ICI model
  - TKI model
- QUANTIFICATION AND STATISTICAL ANALYSIS

SUPPLEMENTAL INFORMATION

Supplemental information can be found online at https://doi.org/10.1016/j.xcrm.2025.102299.

Received: October 9, 2023
Revised: September 13, 2024
Accepted: July 22, 2025
Published: August 19, 2025

REFERENCES

1. Carlo, M.I., Voss, M.H., and Motzer, R.J. (2016). Checkpoint inhibitors and other novel immunotherapies for advanced renal cell carcinoma. Nat. Rev. Urol. *13*, 420–431. https://doi.org/10.1038/nrurol.2016.103.
2. Motzer, R.J., Jonasch, E., Boyle, S., Carlo, M.I., Manley, B., Agarwal, N., Alva, A., Beckermann, K., Choueiri, T.K., Costello, B.A., et al. (2020). NCCN Guidelines Insights: Kidney Cancer, Version 1.2021: Featured Updates to the NCCN Guidelines. J. Natl. Compr. Canc. Netw. *18*, 1160–1170. https://doi.org/10.6004/jnccn.2020.0043.
3. Choueiri, T.K., Powles, T., Burotto, M., Escudier, B., Bourlon, M.T., Zurawski, B., Oyervides Juárez, V.M., Hsieh, J.J., Basso, U., Shah, A.Y., et al. (2021). Nivolumab plus Cabozantinib versus Sunitinib for Advanced Renal-Cell Carcinoma. N. Engl. J. Med. *384*, 829–841. https://doi.org/10.1056/NEJMoa2026982.
4. Motzer, R.J., Penkov, K., Haanen, J., Rini, B., Albiges, L., Campbell, M.T., Venugopal, B., Kollmannsberger, C., Negrier, S., Uemura, M., et al. (2019). Avelumab plus Axitinib versus Sunitinib for Advanced Renal-Cell Carcinoma. N. Engl. J. Med. *380*, 1103–1115. https://doi.org/10.1056/NEJMoa1816047.
5. Motzer, R., Alekseev, B., Rha, S.-Y., Porta, C., Eto, M., Powles, T., Grünwald, V., Hutson, T.E., Kopyltsov, E., Méndez-Vidal, M.J., et al. (2021). Lenvatinib plus Pembrolizumab or Everolimus for Advanced Renal Cell Carcinoma. N. Engl. J. Med. *384*, 1289–1300. https://doi.org/10.1056/NEJMoa2035716.
6. Motzer, R.J., Robbins, P.B., Powles, T., Albiges, L., Haanen, J.B., Larkin, J., Mu, X.J., Ching, K.A., Uemura, M., Pal, S.K., et al. (2020). Avelumab plus axitinib versus sunitinib in advanced renal cell carcinoma: biomarker analysis of the phase 3 JAVELIN Renal 101 trial. Nat. Med. *26*, 1733–1741. https://doi.org/10.1038/s41591-020-1044-8.
7. Braun, D.A., Hou, Y., Bakouny, Z., Ficial, M., Sant' Angelo, M., Forman, J., Ross-Macdonald, P., Berger, A.C., Jegede, O.A., Elagina, L., et al. (2020). Interplay of somatic alterations and immune infiltration modulates

response to PD-1 blockade in advanced clear cell renal cell carcinoma. Nat. Med. *26*, 909–918. https://doi.org/10.1038/s41591-020-0839-y.

8. Tucker, M.D., and Rini, B.I. (2020). Predicting Response to Immunotherapy in Metastatic Renal Cell Carcinoma. Cancers (Basel) *12*, 2662. https://doi.org/10.3390/cancers12092662.
9. McDermott, D.F., Huseni, M.A., Atkins, M.B., Motzer, R.J., Rini, B.I., Escudier, B., Fong, L., Joseph, R.W., Pal, S.K., Reeves, J.A., et al. (2018). Clinical activity and molecular correlates of response to atezolizumab alone or in combination with bevacizumab versus sunitinib in renal cell carcinoma. Nat. Med. *24*, 749–757. https://doi.org/10.1038/s41591-018-0053-3.
10. Rini, B.I., Powles, T., Atkins, M.B., Escudier, B., McDermott, D.F., Suarez, C., Bracarda, S., Stadler, W.M., Donskov, F., Lee, J.L., et al. (2019). Atezolizumab plus bevacizumab versus sunitinib in patients with previously untreated metastatic renal cell carcinoma (IMmotion151): a multicentre, open-label, phase 3, randomised controlled trial. Lancet *393*, 2404–2415. https://doi.org/10.1016/S0140-6736(19)30723-8.
11. Motzer, R.J., Choueiri, T.K., McDermott, D.F., Powles, T., Yao, J., Ammar, R., Papillon-Cavanagh, S., Saggi, S.S., McHenry, B.M., Ross-Macdonald, P., and Wind-Rotolo, M. (2020). Biomarker analyses from the phase III CheckMate 214 trial of nivolumab plus ipilimumab (N+I) or sunitinib (S) in advanced renal cell carcinoma (aRCC). J. Clin. Orthod. *38*, 5009. https://doi.org/10.1200/JCO.2020.38.15_suppl.5009.
12. Motzer, R.J., Banchereau, R., Hamidi, H., Powles, T., McDermott, D., Atkins, M.B., Escudier, B., Liu, L.-F., Leng, N., Abbas, A.R., et al. (2020). Molecular Subsets in Renal Cancer Determine Outcome to Checkpoint and Angiogenesis Blockade. Cancer Cell *38*, 803–817.e4. https://doi.org/10.1016/j.ccell.2020.10.011.
13. Molecular and phenotypic data for patients enrolled in the IMmotion150 trial - EGA European Genome-Phenome Archive https://ega-archive.org/datasets/EGAD00001004183.
14. Raw FASTq files - EGA European Genome-Phenome Archive (IMmotion151) https://ega-archive.org/datasets/EGAD00001006619.
15. Bagaev, A., Kotlov, N., Nomie, K., Svekolkin, V., Gafurov, A., Isaeva, O., Osokin, N., Kozlov, I., Frenkel, F., Gancharova, O., et al. (2021). Conserved pan-cancer microenvironment subtypes predict response to immunotherapy. Cancer Cell *39*, 845–865.e7. https://doi.org/10.1016/j.ccell.2021.04.014.
16. Stupichev, D., Miheecheva, N., Postovalova, E., Lyu, Y., Ramachandran, A., Galkin, I., Khegai, G., Perevoshchikova, K., Love, A., Menshikova, S., et al. (2025). An artificial intelligence-driven algorithm predicts immunotherapy and targeted therapy outcomes in clear cell renal cell carcinoma. (Zenodo). https://doi.org/10.5281/ZENODO.15296474https://doi.org/10.5281/ZENODO.15296474.
17. Turajlic, S., Xu, H., Litchfield, K., Rowan, A., Chambers, T., Lopez, J.I., Nicol, D., O'Brien, T., Larkin, J., Horswell, S., et al. (2018). Tracking Cancer Evolution Reveals Constrained Routes to Metastases: TRACERx Renal. Cell *173*, 581–594.e12. https://doi.org/10.1016/j.cell.2018.03.057.
18. Krishna, C., DiNatale, R.G., Kuo, F., Srivastava, R.M., Vuong, L., Chowell, D., Gupta, S., Vanderbilt, C., Purohit, T.A., Liu, M., et al. (2021). Single-cell sequencing links multiregional immune landscapes and tissue-resident T cells in ccRCC to tumor topology and therapy efficacy. Cancer Cell *39*, 662–677.e6. https://doi.org/10.1016/j.ccell.2021.03.007.
19. Bi, K., He, M.X., Bakouny, Z., Kanodia, A., Napolitano, S., Wu, J., Grimaldi, G., Braun, D.A., Cuoco, M.S., Mayorga, A., et al. (2021). Tumor and immune reprogramming during immunotherapy in advanced renal cell carcinoma. Cancer Cell *39*, 649–661.e5. https://doi.org/10.1016/j.ccell.2021.02.015.
20. Braun, D.A., Street, K., Burke, K.P., Cookmeyer, D.L., Denize, T., Pedersen, C.B., Gohil, S.H., Schindler, N., Pomerance, L., Hirsch, L., et al. (2021). Progressive immune dysfunction with advancing disease stage in renal cell carcinoma. Cancer Cell *39*, 632–648.e8. https://doi.org/10.1016/j.ccell.2021.02.013.
21. Zaitsev, A., Chelushkin, M., Dyikanov, D., Cheremushkin, I., Shpak, B., Nomie, K., Zyrin, V., Nuzhdina, E., Lozinsky, Y., Zotova, A., et al. (2022). Precise reconstruction of the TME using bulk RNA-seq and a machine learning algorithm trained on artificial transcriptomes. Cancer Cell *40*, 879–894.e16. https://doi.org/10.1016/j.ccell.2022.07.006.
22. Miheecheva, N., Postovalova, E., Lyu, Y., Ramachandran, A., Bagaev, A., Svekolkin, V., Galkin, I., Zyrin, V., Maximov, V., Lozinsky, Y., et al. (2022). Multiregional single-cell proteogenomic analysis of ccRCC reveals cytokine drivers of intratumor spatial heterogeneity. Cell Rep. *40*, 111180. https://doi.org/10.1016/j.celrep.2022.111180.
23. Yuen, K.C., Liu, L.-F., Gupta, V., Madireddi, S., Keerthivasan, S., Li, C., Rishipathak, D., Williams, P., Kadel, E.E., Koeppen, H., et al. (2020). High systemic and tumor-associated IL-8 correlates with reduced clinical benefit of PD-L1 blockade. Nat. Med. *26*, 693–698. https://doi.org/10.1038/s41591-020-0860-1.
24. Barbie, D.A., Tamayo, P., Boehm, J.S., Kim, S.Y., Moody, S.E., Dunn, I.F., Schinzel, A.C., Sandy, P., Meylan, E., Scholl, C., et al. (2009). Systematic RNA interference reveals that oncogenic KRAS-driven cancers require TBK1. Nature *462*, 108–112. https://doi.org/10.1038/nature08460.
25. Clark, D.J., Dhanasekaran, S.M., Petralia, F., Pan, J., Song, X., Hu, Y., Da Veiga Leprevost, F., Reva, B., Lih, T.-S.M., Chang, H.-Y., et al. (2019). Integrated Proteogenomic Characterization of Clear Cell Renal Cell Carcinoma. Cell *179*, 964–983.e31. https://doi.org/10.1016/j.cell.2019.10.007.
26. dbGaP Study (CPTAC 3). https://www.ncbi.nlm.nih.gov/projects/gap/cgi-bin/study.cgi?study_id=phs001287.v8.p5.
27. Cancer Genome Atlas Research Network (2013). Comprehensive molecular characterization of clear cell renal cell carcinoma. Nature *499*, 43–49. https://doi.org/10.1038/nature12222.
28. dbGaP Study (TCGA-KIRC). https://www.ncbi.nlm.nih.gov/projects/gap/cgi-bin/study.cgi?study_id=phs000178.v11.p8.
29. Sato, Y., Yoshizato, T., Shiraishi, Y., Maekawa, S., Okuno, Y., Kamura, T., Shimamura, T., Sato-Otsubo, A., Nagae, G., Suzuki, H., et al. (2013). Integrated molecular analysis of clear-cell renal cell carcinoma. Nat. Genet. *45*, 860–867. https://doi.org/10.1038/ng.2699.
30. an integrated molecular study of clear cell renal cell carcinoma (ccRCC) including whole-genome/exome and RNA sequencing as well as array-based gene expression/copy-number/methylation analyses - EGA European Genome-Phenome Archive. https://ega-archive.org/studies/EGAS00001000509.
31. Motzer, R.J., Hutson, T.E., Cella, D., Reeves, J., Hawkins, R., Guo, J., Nathan, P., Staehler, M., De Souza, P., Merchan, J.R., et al. (2013). Pazopanib versus Sunitinib in Metastatic Renal-Cell Carcinoma. N. Engl. J. Med. *369*, 722–731. https://doi.org/10.1056/NEJMoa1303989.
32. COMPARZ - EGA European Genome-Phenome Archive. https://ega-archive.org/datasets/EGAD00010001930.
33. Beuselinck, B., Job, S., Becht, E., Karadimou, A., Verkarre, V., Couchy, G., Giraldo, N., Rioux-Leclercq, N., Molinié, V., Sibony, M., et al. (2015). Molecular Subtypes of Clear Cell Renal Cell Carcinoma Are Associated with Sunitinib Response in the Metastatic Setting. Clin. Cancer Res. *21*, 1329–1339. https://doi.org/10.1158/1078-0432.CCR-14-1128.
34. BioStudies BioStudies < The European Bioinformatics Institute < EMBL-EBI (E-MTAB-3267). https://www.ebi.ac.uk/biostudies/arrayexpress/studies/E-MTAB-3267.
35. Brannon, A.R., Reddy, A., Seiler, M., Arreola, A., Moore, D.T., Pruthi, R.S., Wallen, E.M., Nielsen, M.E., Liu, H., Nathanson, K.L., et al. (2010). Molecular Stratification of Clear Cell Renal Cell Carcinoma by Consensus Clustering Reveals Distinct Subtypes and Survival Patterns. Genes Cancer *1*, 152–163. https://doi.org/10.1177/1947601909359929.
36. Delahunt, B., Cheville, J.C., Martignoni, G., Humphrey, P.A., Magi-Galluzzi, C., McKenney, J., Egevad, L., Algaba, F., Moch, H., Grignon, D.J., et al. (2013). The International Society of Urological Pathology (ISUP) grading system for renal cell carcinoma and other prognostic parameters.

Am. J. Surg. Pathol. *37*, 1490–1504. https://doi.org/10.1097/PAS.0b013e318299f0fb.

37. Radtke, A.J., Postovalova, E., Varlamova, A., Bagaev, A., Sorokina, M., Kudryashova, O., Meerson, M., Polyakova, M., Galkin, I., Svekolkin, V., et al. (2024). Multi-omic profiling of follicular lymphoma reveals changes in tissue architecture and enhanced stromal remodeling in high-risk patients. Cancer Cell *42*, 444–463.e10. https://doi.org/10.1016/j.ccell.2024.02.001.

38. Cabrita, R., Lauss, M., Sanna, A., Donia, M., Skaarup Larsen, M., Mitra, S., Johansson, I., Phung, B., Harbst, K., Vallon-Christersson, J., et al. (2020). Tertiary lymphoid structures improve immunotherapy and survival in melanoma. Nature *577*, 561–565. https://doi.org/10.1038/s41586-019-1914-8.

39. Campbell, K.M., Amouzgar, M., Pfeiffer, S.M., Howes, T.R., Medina, E., Travers, M., Steiner, G., Weber, J.S., Wolchok, J.D., Larkin, J., et al. (2023). Prior anti-CTLA-4 therapy impacts molecular characteristics associated with anti-PD-1 response in advanced melanoma. Cancer Cell *41*, 791–806.e4. https://doi.org/10.1016/j.ccell.2023.03.010.

40. Yfantis, A., Mylonis, I., Chachami, G., Nikolaidis, M., Amoutzias, G.D., Paraskeva, E., and Simos, G. (2023). Transcriptional Response to Hypoxia: The Role of HIF-1-Associated Co-Regulators. Cells *12*, 798. https://doi.org/10.3390/cells12050798.

41. Peña-Llopis, S., Vega-Rubín-de-Celis, S., Liao, A., Leng, N., Pavía-Jiménez, A., Wang, S., Yamasaki, T., Zhrebker, L., Sivanand, S., Spence, P., et al. (2012). BAP1 loss defines a new class of renal cell carcinoma. Nat. Genet. *44*, 751–759. https://doi.org/10.1038/ng.2323.

42. Guo, G., Gui, Y., Gao, S., Tang, A., Hu, X., Huang, Y., Jia, W., Li, Z., He, M., Sun, L., et al. (2011). Frequent mutations of genes encoding ubiquitin-mediated proteolysis pathway components in clear cell renal cell carcinoma. Nat. Genet. *44*, 17–19. https://doi.org/10.1038/ng.1014.

43. Varela, I., Tarpey, P., Raine, K., Huang, D., Ong, C.K., Stephens, P., Davies, H., Jones, D., Lin, M.-L., Teague, J., et al. (2011). Exome sequencing identifies frequent mutation of the SWI/SNF complex gene PBRM1 in renal carcinoma. Nature *469*, 539–542. https://doi.org/10.1038/nature09639.

44. Kroeger, N., Klatte, T., Chamie, K., Rao, P.N., Birkhäuser, F.D., Sonn, G.A., Riss, J., Kabbinavar, F.F., Belldegrun, A.S., and Pantuck, A.J. (2013). Deletions of chromosomes 3p and 14q molecularly subclassify clear cell renal cell carcinoma: *HIF-1α* and *VHL Gene* Deletions in ccRCC. Cancer *119*, 1547–1554. https://doi.org/10.1002/cncr.27947.

45. Lebacle, C.M., Pooli, A., Rao, N., Wood, E.L., Kroeger, N., Liu, S., Faiena, I., Chamie, K., Belldegrun, A.S., Shuch, B., et al. (2019). Prognostic value of gain of chromosome 5q in localized renal cell carcinoma. J. Clin. Orthod. *37*, 623. https://doi.org/10.1200/JCO.2019.37.7_suppl.623.

46. Finke, J.H., Rayman, P., Alexander, J., Edinger, M., Tubbs, R.R., Connelly, R., Pontes, E., and Bukowski, R. (1990). Characterization of the cytolytic activity of CD4+ and CD8+ tumor-infiltrating lymphocytes in human renal cell carcinoma. Cancer Res. *50*, 2363–2370.

47. Schoof, D.D., Terashima, Y., Peoples, G.E., Goedegebuure, P.S., Andrews, J.V., Richie, J.P., and Eberlein, T.J. (1993). CD4+ T cell clones isolated from human renal cell carcinoma possess the functional characteristics of Th2 helper cells. Cell. Immunol. *150*, 114–123. https://doi.org/10.1006/cimm.1993.1183.

48. Angevin, E., Kremer, F., Gaudin, C., Hercend, T., and Triebel, F. (1997). Analysis of T-cell immune response in renal cell carcinoma: polarization to type 1-like differentiation pattern, clonal T-cell expansion and tumor-specific cytotoxicity. Int. J. Cancer *72*, 431–440. https://doi.org/10.1002/(sici)1097-0215(19970729)72:3<431::aid-ijc10>3.0.co;2-f.

49. Giraldo, N.A., Becht, E., Vano, Y., Petitprez, F., Lacroix, L., Validire, P., Sanchez-Salas, R., Ingels, A., Oudard, S., Moatti, A., et al. (2017). Tumor-Infiltrating and Peripheral Blood T-cell Immunophenotypes Predict Early Relapse in Localized Clear Cell Renal Cell Carcinoma. Clin. Cancer Res. *23*, 4416–4428. https://doi.org/10.1158/1078-0432.CCR-16-2848.

50. Brugarolas, J., Rajaram, S., Christie, A., and Kapur, P. (2020). The Evolution of Angiogenic and Inflamed Tumors: The Renal Cancer Paradigm. Cancer Cell *38*, 771–773. https://doi.org/10.1016/j.ccell.2020.10.021.

51. Wang, X.M., Lu, Y., Song, Y.M., et al. (2020). Integrative genomic study of Chinese clear cell renal cell carcinoma reveals features associated with thrombus. Nat Commun *11*, 739. https://doi.org/10.1038/s41467-020-14601-9.

52. von Roemeling, Radisky, D.C., Marlow, L.A., Cooper, S.J., Grebe, S.K., Anastasiadis, P.Z., Tun, H.W., and Copland, J.A. (2014). Neuronal pentraxin 2 supports clear cell renal cell carcinoma by activating the AMPA-selective glutamate receptor-4. Cancer Res *74*, 4796–4810. https://doi.org/10.1158/0008-5472.CAN-14-0210.

53. Wei, X., Choudhury, Y., Lim, W.K., Anema, J., Kahnoski, R.J., Lane, B., Ludlow, J., Takahashi, M., Kanayama, H.O., Belldegrun, A., et al. (2017). Recognizing the Continuous Nature of Expression Heterogeneity and Clinical Outcomes in Clear Cell Renal Cell Carcinoma. Sci Rep *7*, 7342. https://doi.org/10.1038/s41598-017-07191-y.

54. Wozniak, M.B., Le Calvez-Kelm, F., Abedi-Ardekani, B., Byrnes, G., Durand, G., Carreira, C., Michelon, J., Janout, V., Holcatova, I., Foretova, L., et al. (2013). Integrative genome-wide gene expression profiling of clear cell renal cell carcinoma in Czech Republic and in the United States. PloS One *8*, e57886. https://doi.org/10.1371/journal.pone.0057886.

55. Schneider, C., Rasband, W., and Eliceiri, K. (2012). NIH Image to ImageJ: 25 years of image analysis. Nat Methods *9*, 671–675. https://doi.org/10.1038/nmeth.2089.

56. Paszke, A., Gross, S., Massa, F., Lerer, A., Bradbury, J., Chanan, G., Killeen, T., Lin, Z., Gimelshein, N., Antiga, L., et al. (2019). PyTorch: An Imperative Style, High-Performance Deep Learning Library. Preprint at arXiv. https://doi.org/10.48550/arXiv.1912.01703.

57. Andrews, S. (2016). FastQC A Quality Control Tool for High Throughput Sequence Data. Version 0.11.5.

58. Wingett, S.W., and Andrews, S. (2018). FastQ Screen: A tool for multi-genome mapping and quality control. F1000Res. *7*, 1338. https://doi.org/10.12688/f1000research.15931.2.

59. Wang, L., Wang, S., and Li, W. (2012). RSeQC: quality control of RNA-seq experiments. Bioinformatics *28*, 2184–2185. https://doi.org/10.1093/bioinformatics/bts356.

60. Ewels, P., Magnusson, M., Lundin, S., and Käller, M. (2016). MultiQC: summarize analysis results for multiple tools and samples in a single report. Bioinformatics *32*, 3047–3048. https://doi.org/10.1093/bioinformatics/btw354.

61. Szolek, A., Schubert, B., Mohr, C., Sturm, M., Feldhahn, M., and Kohlbacher, O. (2014). OptiType: precision HLA typing from next-generation sequencing data. Bioinformatics *30*, 3310–3316. https://doi.org/10.1093/bioinformatics/btu548.

62. Bergmann, E.A., Chen, B.-J., Arora, K., Vacic, V., and Zody, M.C. (2016). Conpair: concordance and contamination estimator for matched tumor–normal pairs. Bioinformatics *32*, 3196–3198. https://doi.org/10.1093/bioinformatics/btw389.

63. Bushnell, B. (2014). BBMap: A Fast, Accurate, Splice-Aware Aligner (Lawrence Berkeley National Laboratory).

64. Li, H., and Durbin, R. (2009). Fast and accurate short read alignment with Burrows–Wheeler transform. Bioinformatics *25*, 1754–1760. https://doi.org/10.1093/bioinformatics/btp324.

65. Broad Institute Picard Toolkit MarkDuplicates. Version 2.6.0.

66. van der Auwera, G., and O'Connor, B.D. (2020). Genomics in the Cloud: Using Docker, GATK, and WDL in Terra, First edition (O'Reilly Media).

67. Kim, S., Scheffler, K., Halpern, A.L., Bekritsky, M.A., Noh, E., Källberg, M., Chen, X., Kim, Y., Beyter, D., Krusche, P., and Saunders, C.T. (2018). Strelka2: fast and accurate calling of germline and somatic variants. Nat. Methods *15*, 591–594. https://doi.org/10.1038/s41592-018-0051-x.

68. McLaren, W., Gil, L., Hunt, S.E., Riat, H.S., Ritchie, G.R.S., Thormann, A., Flicek, P., and Cunningham, F. (2016). The Ensembl Variant Effect Predictor. Genome Biol. *17*, 122. https://doi.org/10.1186/s13059-016-0974-4.

69. Shen, R., and Seshan, V.E. (2016). FACETS: allele-specific copy number and clonal heterogeneity analysis tool for high-throughput DNA sequencing. Nucleic Acids Res. *44*, e131. https://doi.org/10.1093/nar/gkw520.

70. Favero, F., Joshi, T., Marquard, A.M., Birkbak, N.J., Krzystanek, M., Li, Q., Szallasi, Z., and Eklund, A.C. (2015). Sequenza: allele-specific copy number and mutation profiles from tumor sequencing data. Ann. Oncol. *26*, 64–70. https://doi.org/10.1093/annonc/mdu479.

71. Bray, N.L., Pimentel, H., Melsted, P., and Pachter, L. (2016). Near-optimal probabilistic RNA-seq quantification. Nat. Biotechnol. *34*, 525–527. https://doi.org/10.1038/nbt.3519.

72. Subramanian, A., Tamayo, P., Mootha, V.K., Mukherjee, S., Ebert, B.L., Gillette, M.A., Paulovich, A., Pomeroy, S.L., Golub, T.R., Lander, E.S., and Mesirov, J.P. (2005). Gene set enrichment analysis: A knowledge-based approach for interpreting genome-wide expression profiles. Proc. Natl. Acad. Sci. USA *102*, 15545–15550. https://doi.org/10.1073/pnas.0506580102.

73. Wolf, F., Angerer, P., and Theis, F. (2018). SCANPY: large-scale single-cell gene expression data analysis. Genome Biol *19*, 15. https://doi.org/10.1186/s13059-017-1382-0.

74. Korsunsky, I., Millard, N., Fan, J., Slowikowski, K., Zhang, F., Wei, K., Baglaenko, Y., Brenner, M., Loh, P.R., and Raychaudhuri, S. (2019). Fast, sensitive and accurate integration of single-cell data with Harmony. Nat Methods *16*, 1289–1296. https://doi.org/10.1038/s41592-019-0619-0.

75. Becht, E., McInnes, L., Healy, J., Dutertre, C.A., Kwok, I.W.H., Ng, L.G., Ginhoux, F., and Newell, E.W. (2018). Dimensionality reduction for visualizing single-cell data using UMAP. Nat Biotechnol. https://doi.org/10.1038/nbt.4314.

76. R Core Team (2021). R: A language and environment for statistical computing. R Foundation for Statistical Computing, Vienna, Austria. URL https://www.R-project.org/.

77. Davidson-Pilon, C. (2019). lifelines: survival analysis in Python. J. Open Source Softw. *4*, 1317. https://doi.org/10.21105/joss.01317.

78. Pedregosa, F., Varoquaux, G., Gramfort, A., Michel, V., Thirion, B., Grisel, O., Blondel, M., Prettenhofer, P., Weiss, R., Dubourg, V., et al. (2011). Scikit-learn: Machine Learning in Python. J. Mach. Learn. Res. *12*, 2825–2830.

79. Levine, J.H., Simonds, E.F., Bendall, S.C., Davis, K.L., Amir, el-A.D., Tadmor, M.D., Litvin, O., Fienberg, H.G., Jager, A., Zunder, E.R., et al. (2015). Data-Driven Phenotypic Dissection of AML Reveals Progenitor-like Cells that Correlate with Prognosis. Cell *162*, 184–197. https://doi.org/10.1016/j.cell.2015.05.047.

80. Dobin, A., Davis, C.A., Schlesinger, F., Drenkow, J., Zaleski, C., Jha, S., Batut, P., Chaisson, M., and Gingeras, T.R. (2013). STAR: ultrafast universal RNA-seq aligner. Bioinformatics *29*, 15–21. https://doi.org/10.1093/bioinformatics/bts635.

81. Liao, Y., Smyth, G.K., and Shi, W. The R. (2019). package Rsubread is easier, faster, cheaper and better for alignment and quantification of RNA sequencing reads. Nucleic Acids Res *47*, e47. https://doi.org/10.1093/nar/gkz114.

82. Love, M.I., Huber, W., and Anders, S. (2014). Moderated estimation of fold change and dispersion for RNA-seq data with DESeq2. Genome Biol *15*, 550. https://doi.org/10.1186/s13059-014-0550-8.

83. Korotkevich, G., Sukhov, V., Budin, N., Shpak, B., Artyomov, M.N., and Sergushichev, A. (2019). Fast gene set enrichment analysis. bioRxiv. https://doi.org/10.1101/060012.

84. Bradski, G. (2000). The OpenCV Library. Dr. Dobb's Journal of Software Tools.

85. Shojaei, F., Wu, X., Malik, A.K., Zhong, C., Baldwin, M.E., Schanz, S., Fuh, G., Gerber, H.-P., and Ferrara, N. (2007). Tumor refractoriness to anti-VEGF treatment is mediated by CD11b+Gr1+ myeloid cells. Nat. Biotechnol. *25*, 911–920. https://doi.org/10.1038/nbt1323.

86. De Veirman, K., Van Valckenborgh, E., Lahmar, Q., Geeraerts, X., De Bruyne, E., Menu, E., Van Riet, I., Vanderkerken, K., and Van Ginderachter, J.A. (2014). Myeloid-derived suppressor cells as therapeutic target in hematological malignancies. Front. Oncol. *4*, 349. https://doi.org/10.3389/fonc.2014.00349.

87. Wightman, R., Raw, N., Soare, A., Arora, A., Ha, C., Reich, C., Guan, F., Kaczmarzyk, J., mrT23, Mike, et al. (2023). rwightman/pytorch-image-models: v0.8.10dev0 Release. Version v0.8.10dev0 (Zenodo). https://doi.org/10.5281/zenodo.7618837https://doi.org/10.5281/zenodo.7618837.

88. Pachynski, R.K., Kim, E.H., Miheecheva, N., Kotlov, N., Ramachandran, A., Postovalova, E., Galkin, I., Svekolkin, V., Lyu, Y., Zou, Q., et al. (2021). Single-cell Spatial Proteomic Revelations on the Multiparametric MRI Heterogeneity of Clinically Significant Prostate Cancer. Clin. Cancer Res. *27*, 3478–3490. https://doi.org/10.1158/1078-0432.CCR-20-4217.

89. Veličković, P., Fedus, W., Hamilton, W.L., Liò, P., Bengio, Y., and Hjelm, R. D. (2018). Deep Graph Infomax. Preprint at arXiv. https://doi.org/10.48550/ARXIV.1809.10341.

90. Goldman, M.J., Craft, B., Hastie, M., Repečka, K., McDade, F., Kamath, A., Banerjee, A., Luo, Y., Rogers, D., Brooks, A.N., et al. (2020). Visualizing and interpreting cancer genomics data via the Xena platform. Nat. Biotechnol. *38*, 675–678. https://doi.org/10.1038/s41587-020-0546-8.

91. Liberzon, A., Birger, C., Thorvaldsdóttir, H., Ghandi, M., Mesirov, J.P., and Tamayo, P. (2015). The Molecular Signatures Database Hallmark Gene Set Collection. Cell Syst. *1*, 417–425. https://doi.org/10.1016/j.cels.2015.12.004.

92. Dorogush, A.V., Ershov, V., and Gulin, A. (2018). CatBoost: gradient boosting with categorical features support. Preprint at arXiv. https://doi.org/10.48550/ARXIV.1810.11363.

STAR★METHODS

KEY RESOURCES TABLE

REAGENT or RESOURCE	SOURCE	IDENTIFIER
Antibodies		
CD56 (clone 56C04, same as 123A8)	Thermo Fisher Scientific	MS-1149-P1ABX; RRID:AB_64047
CD4 (clone EPR6855)	Abcam	ab181724; RRID:AB_2864377
NaKATPase (clone EP1845Y)	Abcam	ab167390; RRID:AB_2890241
PCK26 (clone PCK-26)	Sigma	C5992; RRID:AB_2134432
S6 (clone 5G10)	Cell Signaling	58666BC; RRID:AB_331355
CD45 (clone 2B11 + PD7/26)	Dako	M070101-2; RRID:AB_2750582
CD20 (clone EP459Y)	Abcam	ab166865; RRID:AB_1640323
CD206 (clone 5C11)	Sigma	WH0004360M2; RRID:AB_1840543
CD31 (clone 89C2)	Cell Signaling	3528BF; RRID:AB_2160882
PDL1 (clone E1L3N)	Cell Signaling	54601BC; RRID:AB_2687655
HLA DR (clone LN3)	Thermo Fisher Scientific	MS-133-PABX; RRID:AB_63218
CAIX (Polyclonal)	Invitrogen	PA1-16592; RRID:AB_568476
Granzyme B (clone 2C5)	Santa Cruz	sc-8022; RRID:AB_2232723
CD11c (clone D23V1E)	Cell Signaling	45581BF; RRID:AB_2799286
CD8 (clone C8/144B)	Dako	M710301-2; RRID:AB_2075537
CD68 (clone KP1)	Thermo Fisher Scientific	MS397PABX; RRID:AB_720551
CD3 (clone SP7)	Thermo Fisher Scientific	MA5-14524; RRID:AB_10982026
CD16 (clone DJ130c)	Santa Cruz	sc-20052 X; RRID:AB_626925
Ki67 (clone SP6)	Abcam	ab16667; RRID:AB_302459
Chemicals, peptides, and recombinant proteins		
ACK Lysing Buffer	Lonza	Lonza™ 10548E
Fc-receptor blocking solution	Invitrogen	AB_468582
Foxp3/Transcription Factor Staining Buffer Set	eBioscience	00-5523-00
Ir-intercalator	Fluidigm	201192A
KAPA Hyper libraries with xGen Exome Research Panel (v1.0)	IDT	Rxn 10005151
TruSeq Stranded Total RNA	Illumina	20020596
Critical commercial assays		
Tumor Dissociation Kit	Miltenyi Biotec	130-095-929
Deposited data		
TCGA-KIRC	TCGA	https://portal.gdc.cancer.gov/projects/TCGA-KIRC dbGaP accession phs000178.v11.p8; RRID:SCR_003193
JAVELIN Renal 101[6]	Article	Supplementary of https://www.nature.com/articles/s41591-020-1044-8
CPTAC3-Kidney	dbGaP	https://www.ncbi.nlm.nih.gov/projects/gap/cgi-bin/study.cgi?study_id=phs001287.v8.p5; RRID:SCR_00270
IMmotion150	EGA	https://ega-archive.org/datasets/EGAD00001004183; RRID:SCR_004944
IMmotion151	EGA	https://ega-archive.org/datasets/EGAD00001006619; RRID:SCR_004944
ICGC RECA-EU	ICGC	https://platform.icgc-argo.org/; RRID:SCR_021722

(*Continued on next page*)

Continued

REAGENT or RESOURCE	SOURCE	IDENTIFIER
Wang et al., 2020[51]	SRA	https://trace.ncbi.nlm.nih.gov/Traces/sra/?study=SRP238941; RRID:SCR_004891
CheckMate 009/010/025[7]	Article	Supplementary of https://www.nature.com/articles/s41591-020-0839-y
Sato et al., 2013[29]	EGA	https://www.ebi.ac.uk/ega/studies/EGAS00001000509; RRID:SCR_004944
von Roemeling et al., 2014[52]	GEO	https://www.ncbi.nlm.nih.gov/geo/query/acc.cgi?acc=GSE53757; RRID:SCR_005012
Wei et al., 2017[53]	GEO	https://www.ncbi.nlm.nih.gov/geo/query/acc.cgi?acc=GSE73731; RRID:SCR_005012
Wozniak et al., 2013[54]	GEO	https://www.ncbi.nlm.nih.gov/geo/query/acc.cgi?acc=GSE40435; RRID:SCR_005012
IGC's expO	GEO	https://www.ncbi.nlm.nih.gov/geo/query/acc.cgi?acc=GSE2109; RRID:SCR_005012
Beuselinck et al., 2015[33]	EBI	https://www.ebi.ac.uk/arrayexpress/experiments/E-MTAB-3267/
COMPARZ	EGA	https://ega-archive.org/datasets/EGAD00010001930; RRID:SCR_004944
WU-RCC Cohort Sequencing and MxIF Data[16]	Zenodo	https://doi.org/10.5281/zenodo.15296474
Software and algorithms		
ImageJ (Bundled with Java 1.8.0_172)	Schneider et al., 2012[55]	https://imagej.net/; RRID:SCR_003070
PyTorch Python library with UnetResNet-101	Paszke et al., 2019[56]	https://github.com/sshuair/torchsat/tree/develop; RRID:SCR_018536
FastQC (v0.11.5)	Andrews et al., 2016[57]	https://www.bioinformatics.babraham.ac.uk/projects/fastqc/; RRID:SCR_014583
FastQ Screen (v0.11.1)	Wingett and Andrews, 2018[58]	https://www.bioinformatics.babraham.ac.uk/projects/fastq_screen/; RRID:SCR_000141
RSeQC (v3.0.0)	Wang et al., 2012[59]	http://rseqc.sourceforge.net/; RRID:SCR_005275
MultiQC (v1.6)	Ewels et al., 2016[60]	https://github.com/ewels/MultiQC; RRID:SCR_014982
OptiType	Szolek et al., 2014[61]	https://github.com/FRED-2/OptiType; RRID:SCR_022279
Conpair algorithm	Bergmann et al., 2016[62]	http://github.com/nygenome/conpair
FilterByTile/BBMap (v37.90)	Bushnell, 2014[63]	https://jgi.doe.gov/data-and-tools/software-tools/bbtools/bb-tools-user-guide/bbmap-guide/; RRID:SCR_016965
BWA (v0.7.17)	Li and Durbin, 2009[64]	https://github.com/lh3/bwa/releases/tag/v0.7.17; RRID:SCR_010910
Picard MarkDuplicates (v2.6.0)	"Picard Toolkit", 2019. Broad Institute, GitHub Repository.[65]	http://broadinstitute.github.io/picard/; RRID:SCR_006525
GATK (v3.8.1)	Van der Auwera and O'Connor, 2020[66]	https://gatk.broadinstitute.org/hc/en-us; RRID:SCR_001876
Strelka (v2.9)	Kim et al., 2018[67]	https://github.com/Illumina/strelka; RRID:SCR_005109
Variant Effect Predictor (v92.1)	McLaren et al., 2016[68]	https://uswest.ensembl.org/info/docs/tools/vep/index.html; RRID:SCR_007931

(*Continued on next page*)

Continued

REAGENT or RESOURCE	SOURCE	IDENTIFIER
FACETS (v0.5.14)	Shen and Seshan, 2016[69]	https://github.com/mskcc/facets; RRID: SCR_026264
Sequenza (v2.1.2)	Favero et al., 2015[70]	https://github.com/cran/sequenza; RRID: SCR_016662
Kallisto (v0.42.4)	Bray et al., 2016[71]	https://pachterlab.github.io/kallisto; RRID: SCR_016582
ssGSEA	Subramanian et al., 2005[72]	http://software.broadinstitute.org/gsea; RRID:SCR_026610
scanpy Python package	Wolf et al., 2018[73]	https://scanpy.readthedocs.io/en/stable/; RRID:SCR_018139
Harmony	Korsunsky et al., 2019[74]	https://github.com/immunogenomics/harmony; RRID:SCR_022206
UMAP package	Becht et al., 2018[75]	https://github.com/lmcinnes/umap; RRID: SCR_018217
python (v3.7.5)	Python	https://www.python.org/downloads/release/python-375/; RRID:SCR_008394
R (v4.0.2)	R Core Team, 2021[76]	https://cran.r-project.org/; RRID: SCR_001905
lifelines (v0.14.6)	Davidson-Pilon, 2019[77]	https://github.com/CamDavidsonPilon/lifelines/tree/v0.14.6; RRID:SCR_024899
scikit-learn: K-means algorithm	Pedregosa et al., 2011[78]	https://scikit-learn.org/stable/index.html; RRID: SCR_002577
Phenograph	Levine et al., 2015[79]	https://github.com/jacoblevine/PhenoGraph; RRID:SCR_016919
Kassandra™	Zaitsev et al., 2022[21]	https://science.bostongene.com/kassandra/; RRID:SCR_024548
STAR	Dobin et al., 2013[80]	https://github.com/alexdobin/STAR/; RRID:SCR_004463
Rsubread	Liao et al., 2019[81]	https://bioconductor.org/packages/release/bioc/html/Rsubread.html; RRID: SCR_016945
DESeq2	Love et al., 2014[82]	https://github.com/mikelove/DESeq2; RRID:SCR_015687
fgsea	Korotkevich et al., 2019[83]	https://github.com/ctlab/fgsea/; RRID: SCR_020938
TME Classification Algorithm	Bagaev et al., 2021[15]	https://github.com/BostonGene/MFP; RRID:SCR_026873
Cell Atlas MxIF	Miheecheva et al., 2022[22]	https://github.com/BostonGene/Cell_Atlas_MxIF; RRID:SCR_026872
BostonGene/RCC.AI_TKI_IO.Hsieh: Publication Version	Stupichev et al., 2025[16]	https://zenodo.org/records/15580269; RRID:SCR_027035
OpenCV	Bradski et al., 2000[84]	https://opencv.org/; RRID:SCR_015526

METHOD DETAILS

Experimental model and study participant details

WU-RCC cohort collection

The WU-RCC cohort included 193 ccRCC samples collected with informed consent at Washington University School of Medicine in St. Louis under IRB protocol number 201411135 (Table S1, including details on patient age and gender). Patient ages ranged from 19 to 87 years old, with a median age of 60 years. In total, 128 males and 65 females were included in this cohort.

Patients received TKIs (sunitinib, pazopanib, cabozantinib, axitinib; n = 51), ICIs (ipilimumab plus nivolumab; n = 46), or combination ICI+TKI (axitinib plus avelumab, cabozantinib plus nivolumab, axitinib plus pembrolizumab; n = 18) therapies. Additionally, patients with either localized disease after surgery under surveillance (n = 59) or metastatic disease treated with metastasectomy

remaining under active surveillance (AS) without systemic treatment (n = 16) were analyzed. Samples classified as "other" (n = 3) included patients treated with MTOR inhibitors (temsirolimus or everolimus), patients without outcome data, and patients who did not survive prior to therapy initiation.

Cohort selection

Additional open-access cohorts used for this study are listed in Tables S2 and S3, and their identifiers are listed in the key resources table. Details on filtration criteria are illustrated in Figure S2 and Table S3. Briefly, 16 datasets with RNA-seq or microarray data were collected. The gene expression data and clinical annotations were analyzed, the former for batch effect within the reported data and the latter for the exclusion of non-ccRCC cases from subsequent analyses. Datasets containing non-annotated cases of non-ccRCC tumors were also filtered. Samples from unexplained batches were also removed. Among these 16 datasets, seven contained annotations for RECIST or progression-free survival and were therefore used for training and validation of response prediction models. Details on training and validation datasets are illustrated in Figures S5A and S5D.

Pathological examination

Examination of sarcomatoid and rhabdoid features were performed for all cases from the TCGA-KIRC, CPTAC-ccRCC, and WU-RCC cohorts with available histological images by three experienced pathologists. These cases were classified as sarcomatoid, rhabdoid, or non-sarcomatoid based on the WHO/ISUP criteria.[36]

MxIF imaging

Tissue preparation for histology and MxIF imaging

Fresh renal tissue specimens were dissected and fixed in 10% formalin for 48 h at room temperature. Tissue specimens were dehydrated by immersing specimens in a series of ethanol solutions of increasing concentration up to 100% ethanol: 70% (1x), 80% (1x), 95% (1x), 100% (2x) for 1 h each. The specimens were then immersed in fresh xylene (or xylene substitute) three times for 1.5 h each and in paraffin wax (58-60°C) twice for 2 h each. Next, the tissue specimens were embedded into paraffin blocks.

Selection of regions of interest (ROIs)

The tissue regions for MxIF were annotated by an experienced pathologist as normal or tumor based on hemotoxylin and eosin (H&E) staining. The sections imaged were normal, tumor, and normal-tumor interface. For large tumor tissues, different areas of the tissue were included. The ROIs were selected by the pathologist, and the most representative ROIs for each sample were used. Characteristics of the ROIs used for MxIF are listed in Table S5. A total of 34 samples from 34 patients were stained with MxIF and included in this analysis.

Histological examination

Samples were obtained and stored in 10% neutral-buffered formalin until examination. The tissues were embedded in wax, sectioned, and stained using virtual H&E. Virtually stained slides were evaluated by a pathologist, and the fibrotic area was defined as an eosinophilic area of densely packed fibers. The tumor area and intratumoral fibrotic areas were evaluated on a qualitative level. For each H&E slide, 14–20 ROIs covering 2,560 x 2,160 mm each were selected for analysis.

MxIF staining

Tissue sections (5 μm thick) were cut from FFPE ccRCC tissue blocks using a microtome and then mounted onto Superfrost™ Ultra Plus adhesion slides for morphological examination and MxIF analysis. Slide tissue sections were baked at 60°C in an oven for 1 h. Tissue sections were deparaffinized with 2 washes of fresh-xylene and were then rehydrated with washes of 100% ethanol (2x), 95% ethanol (2x), 70% ethanol (2x), 50% ethanol (2x), 1X PBS (1x), and 0.3% Triton X100 in 1X PBS (1x) and subjected to a two-step antigen retrieval process. Next, the tissue sections underwent repeated cycles of staining, imaging, and signal removal. The sections were stained with antibodies directly conjugated with either Cy3 or Cy5 dye at a previously optimized concentration. All antibody mixes used for seven rounds were incubated at room temperature for 1 h in a humid chamber. After incubation , the slides were washed in 1X PBS for 5 min (3X). The tissue sections were stained with DAPI solution (1 ug/mL) for 15 min. The slides were washed with 1X PBS, and the coverslip was applied using mounting media.

MxIF imaging data analysis

Normalized mean expression level analysis

Cell DIVE imaging solution was employed; 10X magnification was used for the virtual H&E images while 20X magnification was used for all the other Cell DIVE images. The images were processed individually, one sample per run. OpenCV2 (https://opencv.org/) code was used to aggregate mean cell expression levels by dividing the marker intensity value inside a contour by the total contour area. For each sample, the expression levels were standardized by removing the mean expression level and scaling to unit variance. Cell typing was performed for each slide individually, which removed the possibility of batch effects. Normalized mean expression levels from 14 out of the 19 markers were used to define cell populations within MxIF micrographs. The markers used were Na,KATPase, PCK26, CAIX, Ki67, CD45, CD3, CD4, CD8, CD20, CD11B, CD11C, CD68, CD206, and CD31 (listed in key resources table). Epithelial cells expressed high levels of PCK26, and a subset stained positive for the Ki67 marker for proliferation. T cells were either $CD3^+$, $CD4^+CD8^+$ double-positive, or single-positive for $CD4^+$ or $CD8^+$ with or without Ki67 staining. B cells were classified as $CD20^+CD45^+$ and then subdivided as Ki67 positive or negative. Macrophages were generally split into groups of $CD68^+CD206^+$ and subpopulations that expressed either $CD68^+$ or $CD206^+$. CD31 marked endothelial cells, while CD45 marked leukocytes. An

additional population of CD11b$^+$ cells was identified with granulocytic morphology that lacked macrophage markers. CD11b is a potential myeloid-derived suppressor cell (MDSC) marker associated with anti-VEGF refractoriness[85] and blocking antitumor host immunity.[86]

Cell segmentation

Cell segmentation was performed using the UNet semantic segmentation neural network with ResNet-101 head from timm library (https://github.com/huggingface/pytorch-image-models),[87] implemented with the PyTorch Python library (https://github.com/pytorch/pytorch).[56] Next, watershed post-processing was applied to the identified cell masks to reduce the under segmented cell counts using the OpenCV2 Python library.[84] Training of the network was performed with manual image segmentation, which consisted of three channels: DAPI, NaKATPase, and S6, with a combination of binary cross entropy and DICE score as loss weighted equally as described in Pachynski et al.[88] Cell quantification of myeloid lineages was performed using CD68, CD206, CD11c, and PDL1 expression levels normalized across samples by the area imaged (Figure 3G). Using this mask- and tessellation-based approach, we evaluated the location and relative abundance of myeloid cells and endothelial cells (Figure 4A). Quantitative tessellation-based imaging revealed myeloid cell types to be far more diverse in cell subpopulations than appreciated by methods employing the cell segmentation only and deconvolution-based approaches due to their complex shape (Figure 4A). We analyzed six tessellation-based subtypes of myeloid cells (CD11C$^+$PDL1$^+$, CD68$^+$CD11C$^+$PDL1$^+$, CD68$^+$CD206$^+$, CD68$^+$CD206$^+$CD11C$^+$PDL1$^+$, CD206$^+$, CD68$^+$, Figure 3G) and 10 mask-based subtypes (tumor, endothelium, CD68, CD206, macrophages, CD68_CD206_CD11C, CD4, CD11C, PDL1, myeloid_PDL1).

Measurement of endothelial cell proximity to CD8$^+$ T cells and macrophages

The distance to the endothelial mask for macrophages and CD8 T cells was computed. First, a distance transformation of the endothelial mask was performed using the OpenCV2 Python package[84] distanceTransform function to generate a map containing the Euclidean distances to the nearest mask pixel. For a given cell of interest, the minimal distance to the endothelial mask was subsequently computed based on the value of the pixel in the distance map located beneath the centroid of the given cell. The distances for macrophages and CD8 T cells were then averaged across the field of view (FOV) and used for downstream statistical analysis.

Cell typing

Cell subtype assignment was performed using Phenograph cell clusterization by standardized mean marker intensity in a given cell contour. Cell subtype assignment was guided by t-SNE plots, which allowed the joining of similar cell subpopulation clusters. Cell typing was visualized by drawing cell contours and coloring them according to cell types.

Eight major cell populations were obtained using the following list of markers: B cells (CD45$^+$, CD19$^+$, CD3$^-$), CD4 T cells (CD45$^+$, CD3$^+$, CD4$^+$, CD8$^-$, CD56$^-$), CD8 T cells (CD45$^+$, CD3$^+$, CD8$^+$, CD4$^-$, CD56$^-$), endothelial cells (CD31$^+$, CD45$^-$), myeloid cells (CD45$^+$, HLADR$^+$, CD68$^+$, CD206$^+$, CD16$^+$, CD11c$^+$), malignant and epithelial cells (CAIX$^+$, NaKATPase$^+$, PCK26$^+$). All unidentified cells and cells with nonspecific annotation were grouped as ''other.''

Community analysis

To perform community detection, graphs of cell to cell interactions were built. Mutual arrangements of cells using Delaunay triangulation for the set of cells' centroids to obtain neighborhood graphs were reconstructed. The upper limit for edge length was set to 200 pixels. For each cell, we identified neighbors as cells on the edges, obtaining neighborhood information in the form of a vector of cell classes and selected mask percentages for each cell. Then, using the resulting graph, the DeepGraphInfomax graph convolutional neural network[89] from the Pytorch Geometric Python package was trained in an unsupervised manner to obtain 32-dimensional embedding of cell neighborhoods in vector form. After this transformation, neighborhood vectors were clustered using the k-means algorithm, obtaining 15 different neighborhood clusters (Figure 4A). For each community cluster, the percentage of cells within a cluster and mask percentage was calculated to facilitate community descriptions. Clusters were grouped based on the dominant cell type proportion and morphological structures into two major groups: tumor-enriched neighborhoods and T cell-enriched neighborhoods. Macrophage-, B-cell-, and blood vessel-enriched neighborhoods were also identified. Cell communities were visualized by drawing cell contours and coloring them according to each community. Community percentages were calculated both in tumor and normal regions or in tumor regions only.

To analyze associations between proportions of communities and ICI/TKI responder scores and similarities among HiTMEs, we calculated correlation between these parameters and expression of 48 cytokines, shown in a clustermap (n = 34; Figure 7D).

Next-generation sequencing (NGS)

Genomic and transcriptomic sequencing was performed using Tempus xT (178 samples) and xR (157 samples) commercially available assays.

WES and RNA-seq

Each pair of tumor and blood (i.e. normal) samples had a single enriched library constructed. Exome libraries were captured by IDT KAPA Hyper libraries with xGen Exome Research Panel v1.0. The libraries were sequenced on an NovaSeq S4 with at least 100x coverage for tumor and 30x for normal. TruSeq Stranded Total RNA (Illumina) was used for RNA library construction. The libraries were sequenced on a NovaSeq S4 with 100 M reads per sample (2 X 150 pairs).

NGS data quality control and analysis

Quality control of all NGS samples was performed using FastQC v0.11.5,[57] FastQ Screen v0.11.1,[58] RSeQC v3.0.0,[59] and MultiQC v1.6.[60] HLA genotypes were calculated from RNA-seq or WES with OptiType.[61] Sample correspondence was checked using HLA comparison and the Conpair algorithm.[62]

DNA sequencing analysis: Alignment and variant calling

Low quality reads were filtered using FilterByTile/BBMap v37.90[63] and aligned to human reference genome GRCh38 (GRCh38.d1.vd1 assembly) using BWA v0.7.17.[64] Duplicate reads were removed using Picard's v2.6.0 MarkDuplicates.[65] Insertions and deletions (INDELs) were realigned by IndelRealigner and recalibrated by BaseRecalibrator and ApplyBQSR with tools from GATK v3.8.1.[66]

Somatic SNVs (sSNVs) and small INDELls were detected using Strelka v2.9.[67] All sSNVs and small INDELs were annotated using Variant Effect Predictor v92.1.[68] The detailed steps are as follows.

Variant calling

Somatic SNVs were detected using optimized Strelka v2.9 on both normal and paired tumor/normal samples, respectively, in exome mode with the default parameters. Somatic INDEL (1-49 bp) calling was performed via Strelka v2.9 using small INDEL candidates from manta v1.5.

Variant filtration

The outputs from the variant calling algorithms underwent subsequent filtration. The output after Strelka2 processing underwent filtration using a basic filter (tumor depth $\geq$ 25 reads, tumor VAF * t_alt_count [read depth supporting the variant allele in tumor] $\geq$ 2). Then, a threshold for tumor VAF $\geq$ 0.05 was applied for single nucleotide polymorphisms (SNPs), double nucleotide polymorphisms (DNPs), and triple nucleotide polymorphisms (TNPs).

CNA analysis

FACETS[69] and Sequenza[70] were used as CNA callers, with refinement and tuning to obtain better quality and speed of calculations. FACETS was used to create a common input file for both the CNA callers. Then, Sequenza generated a resulting file with coverage for each position in .pileup format. Both CNA callers generated the output tables with the number of copies of genome segments.

Mutations in *MTOR* and antigen presentation genes

A list of *MTOR* mutations from OncoKB™ database annotated as "gain of function" or "likely gain of function" was generated and annotated as pathogenic or not according to FATHMM predictions using the COSMIC database. The list contained 88 *MTOR*-activating mutations: A1428T, A1459D, A1459P, A1519T, A1519V, A1971P, A2210P, A2226S, A2420V, A329T, A432V, C1483F, C1483R, C1483W, C1483Y, D2412V, D2512H, E1799K, E2014K, E2288K, E2311*, E2419D, E2419K, E2536A, F1888I, F1888L, F1888V, I1973F, I2500F, I2500M, I2500N, I2501F, K1452N, K1981E, K2507R, L1433S, L1460P, L2172M, L2209V, L2216P, L2220F, L2230V, L2303%3D, L2334V, L2427P, L2427Q, L2427R, L2431P, M2327I, N2211I, P1646S, P2273S, P942S, Q1901*, Q2223K, Q2223R, Q2524L, R1080C, R1203*, R1818C, R2217W, R2505P, R553H, R886C, S2215F, S2215P, S2215T, S2215Y, S2231W, S2328T, T1143M, T1833A, T1977I, T1977K, T1977R, T2232I, T2471M, V2006F, V2006I, V2006L, V2406E, V2406L, V2406M, W1456R, Y1151C, Y1450D, Y1463S, and Y1974H.

To define mutation in antigen presentation genes, an in-depth analysis of *B2M*, *TAP1*, *TAP2*, *CIITA*, *ERAP1*, *ERAP2*, *CANX*, and *CASP8* was performed. A gene was considered mutated if it had one of the following alterations: inframe insertion, inframe deletion, missense mutation, frameshift insertion, frameshift deletion, nonsense mutation, nonstop mutation, or translational start site alteration. For the Javelin RENAL 101 cohort, the list of genes was shortened to *B2M* and *CIITA*, as this cohort lacked information on mutation variant type, with only binary annotation listed as either mutated or wild type.

RNA-seq processing

RNA-seq reads were aligned using Kallisto v0.42.4 to GENCODE v23 transcripts with default parameters.[71] The protein-coding transcripts, IGH/K/L- and TCR-related transcripts were retained, and the noncoding RNA, histone- and mitochondria-related transcripts were removed, resulting in 20,062 protein-coding genes. Gene expression was quantified as transcripts per million (TPM) and log2-transformed.[90]

Deconvolution of bulk RNA-seq

Machine learning algorithm Kassandra was used to predict cell percentages from bulk RNA-seq.[21]

Gene signature score calculations

The ssGSEA scores were calculated using a modified formula from Barbie et al.[24] Raw scores were medium scaled to (-2, 2) or to (-3, 3) range.

Differential expression analysis

RNA-seq data was aligned on the genome by STAR v2.4.2a. GRCh38.d1.vd1 reference sequence and indexes were downloaded from https://gdc.cancer.gov/about-data/data-harmonization-and-generation/gdc-reference-files, GENCODE v22. Gene counts were quantified by Rsubread. Differential expression analysis was carried out using the DESeq2 package. CR and PR patients (responders) were compared with SD and PD (non-responders). Differentially expressed genes (DEGs) were used for gene set enrichment analysis (GSEA) by fgsea in a collection of hallmarks and canonical pathways from Molecular Signatures Database (MsigDB).[72,91]

Myogenesis and ECM signature calculation

Genes for myogenesis and ECM signatures were obtained by GSEA of DEGs from responders versus non-responders among ccRCC patients treated with ICI or combination (Table S6). Genes from the raw ECM signature were filtered according to the rule that the median gene expression should be more than 1 TPM in at least two datasets. Following analysis included calculation of ssGSEA scores and scaling the scores inside the cohorts. These signatures were not used for HiTME subtype identification.

TME subtype identification

Gene expression was harmonized from various platforms: Illumina RNA-seq, Affymetrix GeneChip Human Gene 1.0 ST Array, Affymetrix Human Transcriptome Array 2.0, Affymetrix GeneChip Human Genome U133 Plus 2.0 Array, Illumina HumanHT-12 V4.0 expression beadchip. If the data were derived from expression arrays, we calculated expressions using standard packages. affygcRMA and oligo R packages were used to reprocess the raw files when possible. The Affymetrix datasets with CEL files were re-normalized using the gcRMA package with default parameters. Illumina array data were downloaded from GEO without additional processing. If multiple probes matched one gene during microarray data pre-processing, the probe with the highest mean expression across the cohort was selected for all samples in the cohort. Expression from RNA-seq data was calculated using our pipeline, which measures gene expression using TPM units. When raw data was not available, fragments per kilobase of transcript per million reads mapped (FPKM) or reads per kilobase of transcript per million reads mapped (RPKM) values were utilized. For all cohorts, we selected only ccRCC samples, and all other histological types and normal samples were excluded. In total, we developed a meta-cohort of 3,621 ccRCC samples from 14 datasets. We used 33 gene signatures to identify our HiTME subtypes (Table S4). The activity of each signature in each sample was measured using the ssGSEA algorithm. The ssGSEA scores were calculated using a modified formula from Barbie et al.[24]

The ssGSEA scores for each signature were scaled inside each batch using modified z-score with the median instead mean and median absolute deviation instead standard deviation. After that, we generated a graph in which the nodes represented samples and the edges represented the correlation of the ssGSEA scores. Each node had 120 neighbors. The Leiden algorithm was applied to the resulting graph, defining the five clusters or "HiTME subtypes." The similarity of a sample to a particular HiTME subtype was calculated as the Spearman correlation coefficient between the sample's ssGSEA scores for 33 signatures and the unique HiTME subtypes' averaged ssGSEA scores from the same signatures described here (Table S7).

The WU-RCC and COMPARZ cohorts were used only for HiTME subtype validation. These samples were classified using the k-nearest neighbors classifier from the scikit-learn library[78] based on the resulting meta-cohort clusters.

scRNA-seq analysis

The Scanpy Python package was used to analyze single-cell gene expression from three ccRCC datasets: phs002065.v1.p1, phs002252.v1.p1, and PRJNA705464.[18–20] Following harmony batch correction between datasets, Leiden clustering was applied. Cell types were annotated on the basis of known cell markers and initial dataset annotations. Then, a number of FGESs were calculated, averaged by cell type, and scaled separately within each dataset. After, the data was united, and an averaged heatmap was plotted.

ICI model

To select features for the ICI response model, we created a clustermap of 43 transcriptomic features, including 33 gene signatures used for HiTME identification, an ECM signature found in differential expression analysis, *PDCD1* (PD1) and *CD274* (PDL1) gene expression, and similarities to each of the five portraits: similarity(IE/M), similarity(IE), similarity(F), similarity(D), and similarity(V). The clustermap contained six clusters. One feature from each cluster was selected, resulting in a list of six features: fatty acid metabolism, *CD274* (PDL1) and *PDCD1* (PD1) expression, difference between similarity to the IE portrait and similarity to the F portrait (similarity[IE] - similarity[F]), angiogenesis, proliferation rate, and ECM-associated signature.

We trained a model for every possible combination of features from the aforementioned list. We used the CatBoost classifier model[92] with the "auto_class_weights" parameter set to "balanced." We trained the ICI model on samples treated with ICI-containing regimes from three cohorts: IMmotion151 (n = 362 patients treated with atezolizumab plus bevacizumab), IMmotion150 (n = 75 patients treated with atezolizumab, n = 79 patients treated with atezolizumab plus bevacizumab), and CheckMate 009/010/025 (n = 172 patients treated with nivolumab) for a total of 688 samples. For model training, we selected patients from these three cohorts with CR (n = 40 patients) and PD (n = 190 patients) by RECIST criteria (total n = 230 patients; Figures 5A and S6A). After training on CR and PD patient samples, the model was used to calculate ICI response scores for PR and SD patients as well.

To select the best model, we calculated several parameters for every model performance: crossvalue_score, *p* value from the survival logrank test for CheckMate 009/010/025 and IMmotion151 datasets, p-value from Mann–Whitney *U* test between PR and SD samples for IMmotion150 and IMmotion151 (Table S8). Combining PDL1 and PD1 expressions, similarity(IE) - similarity(F), angiogenesis, proliferation rate, and ECM-associated features yielded the best parameters: high crossvalue score (>0.7) and significant *p* value (<0.05) from both logrank test and Mann–Whitney *U* test in at least one dataset.

In addition, we identified a group of biomarkers that were strongly associated with nonresponse to ICI regimens. Patients with these biomarkers were annotated as "molecular ICI nonresponders" ("molecular ICI NRs"). Samples were classified as molecular ICI NRs if they met at least one of the following criteria: high myogenesis signature (median-scaled gene signature score >15),

mTOR-activating mutations, or mutations in antigen presentation machinery. Samples classified as "molecular ICI nonresponders" were automatically assigned a responder score of 0 and excluded from the final model training and validation.

The final ICI model was trained on transcriptomic features: mean scaled expression of *CD274* (PDL1) and *PDCD1* (PD1); angiogenesis, ECM-associated, and proliferation rate FGESs; and similarity(IE) - similarity(F). We trained our model with CR versus PD on several training cohorts as described above. After training, our model predicted response scores for PR and SD in the training cohorts. The training cohorts included:

(1) IMmotion150 samples (n = 75) treated with atezolizumab, which consisted of 9 CRs, 8 PRs (+1 "molecular ICI NR"), 25 SDs (+7 "molecular ICI NRs"), and 22 PDs (+3 "molecular ICI NRs").
(2) IMmotion150 samples (n = 79) treated with atezolizumab and bevacizumab, composed of 7 CRs, 19 PRs (+2 "molecular ICI NRs"), 22 SDs (+5 "molecular ICI NRs"), and 21 PDs (+3 "ICI molecular NRs").
(3) IMmotion151 samples (n = 362) treated with atezolizumab and bevacizumab with 23 CRs; 122 PRs (+1 "molecular ICI NR"); 143 SDs (+3 "molecular ICI NRs"), and 70 PDs.
(4) CheckMate 009/010/025 samples (n = 172) treated with nivolumab with 1 CR, 38 PRs, 60 SDs (+4 "molecular ICI NRs"), and 61 PDs (+8 "molecular ICI NRs").

Validation was performed with the following cohorts:

(1) JAVELIN Renal 101 samples (n = 337) treated with avelumab plus axitinib, which contained 270 patients and 67 "molecular ICI NRs." RECIST annotation was not available.
(2) WU-RCC samples (n = 37) treated with ipilimumab and nivolumab with 5 CRs (+1 "molecular ICI NR"), 6 PRs, 9 SDs (+1 "molecular ICI NR"), and 10 PDs (+5 "molecular ICI NRs").
(3) WU-RCC samples (n = 12) treated with either cabozantinib plus nivolumab, axitinib plus pembrolizumab, axitinib plus avelumab, with 3 CRs, 6 PRs, 2 SDs, and 0 PDs (+1 "molecular ICI NR").
(4) E-MTAB-3218 samples (n = 44) treated with nivolumab with 2 CRs, 4 PRs, 22 SDs (+1 "molecular ICI NRs"), 12 PDs (+1 "molecular ICI NRs"), and 2 NEs.

We analyzed the distribution of obtained ICI scores on validation samples and split scores into three groups. ICI responder scores greater than 0.4 (third quartile) were considered high based on the upper quartile of the response score distribution, while scores less than 0.1 (First quartile) were considered low based on the lower quartile of the score distribution. Response scores between 0.1 and 0.4 (within first and third quartiles) were classified as medium ICI responder scores.

TKI model

Using the Boruta-SHAP algorithm from the set of 33 transcriptomic signatures used for HiTME identification, the set that gives the best result in predicting response to treatment was selected: angiogenesis, regulatory T-cell traffic, macrophages, proliferation rate, and cyclic nucleotide metabolism (Table S7). Next, the minimum set (macrophages, angiogenesis, and proliferation rate) of uncorrelated features that can be biologically substantiated was selected.

We used a logistic regression model from the scikit-learn package[78] with default parameters. The model was trained based on three transcriptomic features: macrophages, angiogenesis and proliferation rate gene signatures. TKI-treated samples were taken from two cohorts: IMmotion151 (206 patients treated with sunitinib) and E-MTAB-3267 (34 patients treated with sunitinib). For model training, we separated patients from these cohorts into two classes: combined CR and PR patients as responders and PD patients as non-responders. We validated our model on JAVELIN Renal 101 cohort (364 patients treated with sunitinib), COMPARZ (341 patients treated with sunitinib and pazopanib), IMmotion150 (79 patients treated with sunitinib), and WU-RCC (38 patients treated with sunitinib, pazopanib, cabozantinib, and axitinib). SD patients from IMmotion151 (n = 159), and E-MTAB-3267 (n = 19) were not used for model training, but they were included in all plots.

We analyzed the distribution of obtained TKI scores on validation samples and split scores into three groups. The resulting model score varied from 0 to 1. TKI responder scores >0.80 (corresponds to the third quartile of the scores distribution) were classified as high. TKI responder scores <0.55 (corresponds to the first quartile of the scores distribution) were considered low. TKI responder scores ranging from 0.55 to 0.80 were classified as medium.

QUANTIFICATION AND STATISTICAL ANALYSIS

For statistical analyses and plotting, python (version 3.7.5) and R (version 4.0.2) were used. The statistical information is detailed in the text, figure legends, and figures. Significance values correspond to p values as follows: '-' > 0.05, * <0.05, ** <0.01, *** <0.001. To compare non-categorical values between groups we used the Mann–Whitney U test. In the boxplots, the upper whisker indicates the maximum value or 75th percentile +1.5 IQR; the lower whisker indicates the minimum value or 25th percentile −1.5 IQR. Survival differences were assessed using pairwise or multivariate logrank test CamDavidsonPilon/lifelines: v0.14.6.[77]